

The importance of alkyl nitrates and sea ice emissions to atmospheric NO_x sources and cycling in the summertime Southern Ocean marine boundary layer

Jessica Mary Burger¹, Julie Granger², Emily Joyce³, Meredith Galanter Hastings³, Kurt Angus McDonald Spence¹, Katy Elisabeth Altieri¹

¹Department of Oceanography, University of Cape Town, Rondebosch, 7701, South Africa

²Department of Marine Sciences, University of Connecticut, Groton, 06340, USA

³Department of Earth, Environmental and Planetary Sciences and Institute at Brown for Environment and Society, Brown University, Providence, RI, 02906, USA.

Correspondence to: Jessica M. Burger (brgjes006@uct.ac.za)

Abstract. Atmospheric nitrate originates from the oxidation of nitrogen oxides ($\text{NO}_x = \text{NO} + \text{NO}_2$) and impacts both tropospheric chemistry and climate. NO_x sources, cycling, and NO_x to nitrate formation pathways are poorly constrained in remote marine regions, especially the Southern Ocean where pristine conditions serve as a useful proxy for the preindustrial atmosphere. Here, we measured the isotopic composition ($\delta^{15}\text{N}$ and $\delta^{18}\text{O}$) of atmospheric nitrate in coarse-mode ($> 1\mu\text{m}$) aerosols collected in the summertime marine boundary layer of the Atlantic Southern Ocean from 34.5°S to 70°S , and across the northern edge of the Weddell Sea. The $\delta^{15}\text{N}\text{-NO}_3^-$ decreased with latitude from -2.7‰ to -42.9‰ . The decline in $\delta^{15}\text{N}$ with latitude is attributed to changes in the dominant NO_x sources: lightning at the low latitudes, oceanic alkyl nitrates at the mid latitudes, and photolysis of nitrate in snow at the high latitudes. There is no evidence of any influence from anthropogenic NO_x sources or equilibrium isotopic fractionation. Using air mass back trajectories and an isotope mixing model, we calculate that oceanic alkyl nitrate emissions have a $\delta^{15}\text{N}$ signature of $-21.8\text{‰} \pm 7.6\text{‰}$. Given that measurements of alkyl nitrate contributions to remote nitrogen budgets are scarce, this may be a useful tracer for detecting their contribution in other oceanic regions. The $\delta^{18}\text{O}\text{-NO}_3^-$ was always less than 70‰ , indicating that daytime processes involving OH are the dominant NO_x oxidation pathway during summer. Unusually low $\delta^{18}\text{O}\text{-NO}_3^-$ values (less than 31‰) were observed at the western edge of the Weddell Sea. The air mass history of these samples indicates extensive interaction with sea ice covered ocean, which is known to enhance peroxy radical production. The observed low $\delta^{18}\text{O}\text{-NO}_3^-$ is therefore attributed to increased exchange of NO with peroxy radicals, which have a low $\delta^{18}\text{O}$, relative to ozone, which has a high $\delta^{18}\text{O}$. This study reveals that the mid- and high-latitude surface ocean may serve as a more important NO_x source than previously thought, and that the ice-covered surface ocean impacts the reactive nitrogen budget as well as the oxidative capacity of the marine boundary layer.

29 **1 Introduction**

30 Atmospheric nitrate (NO_3^-), hereafter defined as gas phase nitric acid (HNO_3) and particulate NO_3^- (p- NO_3^-), impacts air quality
31 and climate by contributing to atmospheric particulate matter (Park and Kim, 2005), and influencing the Earth's radiative heat
32 budget (IPCC, 2013). It also plays a major role in the biogeochemical cycling of reactive nitrogen (Altieri et al., 2021). NO_3^-
33 aerosols originate from the oxidation of nitrogen oxides, collectively referred to as NO_x ($\text{NO}_x = \text{NO} + \text{NO}_2$). NO_x cycling
34 controls the chemical production of tropospheric ozone (O_3), a greenhouse gas and pollutant (Finlayson-Pitts and Pitts, 2000),
35 which in turn contributes to the oxidising capacity of the atmosphere (Alexander and Mickley, 2015). Globally, fossil fuel
36 combustion is the primary NO_x source (van der A et al., 2008), which far exceeds natural emissions such as biomass burning
37 (Finlayson-Pitts and Pitts, 2000), soil processes (Davidson and Kinglerlee, 1997) and lightning (Schumann and Huntrieser,
38 2007).

39 Due to its remoteness, the summertime Southern Ocean (SO) marine boundary layer (MBL) can be representative of
40 preindustrial-like atmospheric conditions (Hamilton et al., 2014). The chemical composition of the Southern Ocean MBL is
41 characterised by low NO_3^- concentrations (Virkkula et al., 2006), representative of a background aerosol environment (i.e.,
42 minimal anthropogenic influence). Furthermore, the South Atlantic sector of the Southern Ocean is primarily influenced by
43 natural NO_x sources. During summer, high lightning activity over South America and southern Africa results in NO_x production
44 between approximately 40° S and the intertropical convergence zone (ITCZ) (Nesbitt et al., 2000). As such, lightning is
45 expected to be the dominant NO_x source in the low latitude MBL (Schumann and Huntrieser 2007, van der A et al., 2008).
46 Because of its pristine nature, the summertime Southern Ocean serves as a unique region in which to study atmospheric
47 chemistry and is a useful preindustrial reference point for comparing the magnitude of anthropogenic aerosol impacts on
48 climate (Haywood and Boucher 2000; Hamilton et al., 2014).

49 The atmospheric chemistry of the polar MBL at the high southern latitudes differs from that of the mid- and low-latitude
50 MBL. During summer, high levels of photochemistry result in the emission of reactive gases from sea ice and snow cover in
51 the Antarctic. As a result, highly elevated concentrations of hydrogen oxide radicals ($\text{HO}_x = \text{OH} + \text{peroxy radicals}$), halogens,
52 nitrous acid (HONO), and NO_x have been observed during spring and summer in the polar regions (Brough et al., 2019).
53 Furthermore, photochemical production of NO_x within the surface snow of Antarctica and subsequent oxidation in the
54 overlying atmosphere represents a significant NO_3^- source to the Antarctic troposphere (Jones et al., 2000, 2001). NO_3^-
55 photolysis near the surface-air interface of ice crystals produces NO_2 (Grannas et al. 2007; Jones et al., 2000), which can be
56 released to the firn (i.e., the intermediate stage of ice between snow and glacial ice) air and escape the snowpack to the
57 overlying atmosphere (Erbland et al., 2013; Shi et al., 2015; Shi et al., 2018). During winter, additional NO_x sources to the
58 Antarctic atmosphere may include long-range transported peroxyacetyl nitrates (PAN) and stratospheric inputs (Savarino et
59 al., 2007; Lee et al., 2014; Walters et al., 2019).

60 Emission of alkyl nitrates (a group of nitrogen gases collectively referred to as RONO_2) from the surface ocean have been
61 recently proposed as a potential NO_x source to the MBL in remote regions (Williams et al., 2014; Fisher et al., 2018).

62 Observations of elevated MBL alkyl nitrate concentrations suggest that a direct oceanic source exists in both the tropics (Atlas
63 et al., 1993; Blake et al., 2003), and the high-latitude Southern Ocean (Blake et al., 1999; Jones et al., 1999). Although the
64 exact mechanism remains unclear, experimental evidence suggests that oceanic RONO₂ production occurs via photochemical
65 processes involving the aqueous phase reaction of RO₂, derived from the photolysis of oceanic dissolved organic matter and
66 NO, derived from seawater nitrite photolysis (Dahl et al., 2003; Dahl and Saltzman, 2008). Supersaturated RONO₂ conditions
67 in the surface ultimately drive a net flux from the ocean to the atmosphere (Chuck et al., 2002; Dahl et al., 2005). The photolysis
68 of emitted RONO₂ and subsequent OH oxidation in the overlying atmosphere leads to NO_x formation (Fisher et al., 2018), and
69 /or RONO₂ can form aerosol NO₃⁻ directly by hydrolysis (Rindelaub et al., 2015).

70 Current global atmospheric models suggest that oceanic RONO₂ represents a significant source of nitrogen (N) to the
71 Southern Ocean MBL, accounting for 20% to 60% of the reactive N pool at the high-latitudes (60° S to 90° S) (Fisher et al.,
72 2018). However, only one shipborne dataset with coincident ocean-atmosphere RONO₂ concentration measurements exists to
73 substantiate this notion (Hughes et al., 2008). Additionally, the NO_x source from RONO₂ degradation dominates relative to
74 model defined primary NO_x emission sources over the SO, which include shipping, aircraft and lightning (Fisher et al., 2018).
75 However, the lack of seawater observations available to constrain Southern Ocean RONO₂ distributions hamper the validation
76 of model fluxes. Better understanding of the Southern Ocean RONO₂ source is required to improve simulations and accurately
77 evaluate its contribution to the Southern Ocean MBL NO_x budget.

78 **1.1 Natural abundance isotopes of atmospheric nitrate**

79 Measurements of the oxygen (O) and N stable isotope ratios of atmospheric NO₃⁻ can be used to constrain NO_x sources, NO-
80 NO₂ cycling, and NO_x to NO₃⁻ oxidation pathways, which are critical for understanding the reactive N budget in the
81 atmosphere. This technique has been applied in polluted (Elliot et al., 2007; Zong et al., 2017), open ocean (Hastings et al.,
82 2003; Morin et al., 2009; Kamezaki et al., 2019; Gobel et al., 2013; Altieri et al., 2013), and polar environments (Morin et al.,
83 2009; Walters et al., 2019). Stable isotope ratios are reported as a ratio of the heavy to light isotopologues of a sample relative
84 to the constant isotopic ratio of a reference standard, using delta (δ) notation in units of “per mil” (‰) following Eq. (1):

$$85 \quad \delta = \left(\frac{R_{sample}}{R_{standard}} - 1 \right) \times 1000 \quad (1)$$

86 where *R* represents the ratio of ¹⁵N/¹⁴N or ¹⁸O/¹⁶O in the sample and in the reference standard, respectively. The reference for
87 O is Vienna Standard Mean Ocean Water (VSMOW) and for N is atmospheric N₂ (Böhlke et al., 2003).

88 When NO_x is converted to NO₃⁻, the N atom is conserved. As such, it is generally expected that the N stable isotope ratio
89 of atmospheric NO₃⁻ (δ¹⁵N-NO₃⁻) reflects the δ¹⁵N of the source NO_x, (Kendall et al., 2007) plus any isotopic fractionation
90 associated with NO/NO₂ cycling or NO_x to NO₃⁻ conversion. For example, the δ¹⁵N of lightning generated NO_x is close to 0‰
91 (Hoering, 1957) and is distinct from stratospheric and snowpack NO_x. Savarino et al., (2007) used the degree of N₂O
92 destruction in the stratosphere and the associated isotopic fractionation to derive an Antarctic stratospheric δ¹⁵N-NO_x source
93 signature of 19‰ ± 3‰ (Savarino et al., 2007). In contrast, snow emitted NO_x typically has a very low δ¹⁵N signature due to

94 the large fractionation ($^{15}\epsilon$) of $\sim -48\%$ (Berhanu et al., 2014, 2015) associated with NO_3^- photolysis in the snowpack, where
95 $^{15}\epsilon = (\text{KIE} - 1) \times 1000\%$ and the kinetic isotope effect (KIE) is the ratio of the rates with which the two isotopes of N are
96 converted from reactant to product. If equilibrium isotope fractionation during NO/NO_2 cycling occurs, it results in the ^{15}N
97 enrichment of NO_2 such that the NO_3^- formed from this NO_2 will have a higher $\delta^{15}\text{N}-\text{NO}_3^-$ than the initial NO_x source (Freyer
98 et al., 1993; Walters et al., 2016). Equilibrium isotope fractionation during the transformation of NO_x to NO_3^- also results in
99 higher $\delta^{15}\text{N}-\text{NO}_3^-$ compared to the original NO_x source (Walters and Michalski, 2015).

100 In contrast to N, the O stable isotope ratio of atmospheric NO_3^- ($\delta^{18}\text{O}-\text{NO}_3^-$) is reflective of the oxidants involved in NO_x
101 cycling prior to NO_3^- formation, as well as the dominant NO_3^- formation pathway (Hastings et al., 2003; Michalski et al., 2003;
102 Alexander et al., 2020). The O atoms of NO_x are rapidly exchanged with oxidising agents in the atmosphere to produce NO_3^- .
103 Tropospheric NO_x recycles rapidly with O_3 following the equations below:



106 The oxidation of NO to NO_2 requires an atmospheric oxidant, typically O_3 throughout most of the troposphere (R1), while the
107 breakdown of NO_2 back to NO is photolytic and requires light (R2). Therefore, under nighttime/dark conditions (R2) shuts
108 down and NO_x is comprised almost entirely of NO_2 .

109 The dominant daytime sink for NO_x is the oxidation of NO_2 by OH , which produces nitric acid (HNO_3) via (R3), where M is
110 a non-reacting molecule.



112 Under nighttime/dark conditions, the photolytic production of OH cannot occur and NO_2 is oxidised by O_3 (R4). HNO_3 is
113 ultimately formed via the hydrolysis of dinitrogen pentoxide (N_2O_5), following the reactions (R5) and (R6) below:



117 NO_3 can also react with hydrocarbons (HC) (e.g., dimethylsulphide (DMS)) to form HNO_3 following reaction (R7) below:



119 Lastly, in regions with elevated halogen concentrations, NO_2 can be oxidised by reactive halogens, for example bromine oxide
120 (BrO), to form HNO_3 following (R8) and (R9) below:



123 Typically, aerosol $\delta^{18}\text{O}-\text{NO}_3^-$ is interpreted as being determined by the dominant NO_x oxidation pathways, (R3) versus
124 (R4) to (R9). If some combination of R4-R9 occurs, then O_3 is the main oxidant, whereas during (R3), one of the O atoms
125 originates from OH . The OH radical exchanges with H_2O vapor in the troposphere, therefore the $\delta^{18}\text{O}$ of OH is a function of
126 the $\delta^{18}\text{O}$ of H_2O vapour, which generally ranges from -27.5% to 0% in the subtropics and over the Southern Ocean (Michalski
127 et al., 2012; Guilpart et al., 2017; Dar et al., 2020), and equilibrium isotope exchange between OH and H_2O (Walters and

128 Michalski, 2016). In contrast the $\delta^{18}\text{O}$ of tropospheric O_3 is much higher, the most recent estimate being $114.8 \pm 10.4\%$ (Vicars
129 and Savarino, 2014). Therefore, a higher $\delta^{18}\text{O}$ for atmospheric NO_3^- reflects the increased influence of O_3 on NO_x to NO_3^-
130 conversion (R4-R9), and the $\delta^{18}\text{O}-\text{NO}_3^-$ is lower when (R3) is favoured, due to the lack of exchange of O atoms with O_3
131 (Hastings et al., 2003; Fang et al., 2011; Altieri et al., 2013).

132 Here, we present the concentration and isotopic composition of coarse mode ($> 1 \mu\text{m}$) atmospheric NO_3^- collected in the
133 MBL of the Southern Ocean between Cape Town, South Africa and coastal Antarctica, as well as across the Weddell Sea gyre,
134 during summer. Using air mass back trajectories, surface ocean nitrite measurements, and the aerosol $\delta^{15}\text{N}$ - and $\delta^{18}\text{O}-\text{NO}_3^-$,
135 we address 1) the major NO_x sources as well as the main oxidants in NO/NO_2 cycling and NO_x to NO_3^- conversion across a
136 large latitudinal transect of the Atlantic Southern Ocean and within the Weddell Sea gyre, and 2) the influence of sea-ice and
137 snowpack emissions on $\text{NO}_x/\text{NO}_3^-$ chemistry in the high-latitude MBL.

138 2) Methods

139 2.1) Sample collection

140 Samples were collected on board the Research Vessel (R/V) *SA Agulhas II* during one cruise subdivided into three legs. Leg
141 one refers to the voyage south from Cape Town (33.9°S , 18.4°E) to Penguin Bukta (71.4°S , 2.5°W) in early summer (7 to
142 19 December 2018) as part of the South African National Antarctic Expedition's annual relief voyage (SANAE 58). Leg two
143 is the Weddell Sea Expedition (WSE) from 4 January to 21 February 2019. All data were recorded in GMT. The WSE refers
144 to the voyage west from Penguin Bukta to the northern edge of the Weddell Sea gyre to Larsen C ice shelf, followed by a
145 detour to King George Island before returning to the Weddell Sea and sailing back to Penguin Bukta. Leg three refers to the
146 SANAE 58 return voyage north from Penguin Bukta to Cape Town in late summer (27 February to 15 March 2019). From
147 here on, legs one, two and three will be referred to as early summer, the Weddell Sea, and late summer, respectively.

148 Size-segregated atmospheric aerosols were collected on the ninth floor above the bridge (approximately 20 m above sea
149 level), using a high-volume air sampler (HV-AS; Tisch Environmental). Air was pumped at an average flow rate of 0.82 m^3
150 min^{-1} through a five-stage cascade impactor (TE-235; Tisch Environmental), loaded with combusted (400°C for 4 hours) glass
151 fibre filters (TE-230-GF; Tisch Environmental) that have a surface area of approximately 119 cm^2 . Aerosol nitrate in the MBL
152 is predominantly present in the coarse mode ($> 1 \mu\text{m}$), therefore only filter stages 1 through 4 were analysed, where the
153 aerodynamical diameter of particles collected are as follows: stage 1 ($> 7 \mu\text{m}$); stage 2 (3 to $7 \mu\text{m}$); stage 3 (1.5 to $3 \mu\text{m}$) and
154 stage 4 (1 to $1.5 \mu\text{m}$).

155 A sector collector was used to restrict HV-AS activity to avoid contamination from ship stack emissions (Campbell
156 Scientific Africa). The HV-AS only began operating if the wind was blowing at an angle less than 75° or greater than 180°
157 from the bow of the ship for a minimum of ten minutes at a speed of at least 1 m s^{-1} . Filters were removed from the cascade
158 impactor inside a laminar flow cabinet (Air Science), placed in individual zip-sealed plastic bags and stored at -20°C until
159 analysis.

160 Given that the MBL of the Southern Ocean is characterised by low atmospheric NO_3^- concentrations, an attempt was made
161 to ensure that at least 24 hours of in-sector sampling had passed before filters were removed from the cascade impactor.
162 However, this was not always possible as on occasion the filters had to be removed early to avoid contamination due to unusual
163 ship manoeuvres or stagnant conditions. Therefore, sampling times ranged between 13 and 88 hours across the three legs. The
164 details of each cruise leg can be found in the supplemental information (Table S1).

165 During the research voyage, a field blank was collected by fitting the cascade impactor with a set of filters and walking the
166 cascade impactor from the laboratory to the HV-AS in the same way that atmospheric samples were deployed. The cascade
167 impactor was placed into the HV-AS and then immediately removed without the HV-AS turning on, after which the filters
168 were removed from the cascade impactor and stored in the same manner as the atmospheric samples. All chemical analyses
169 performed on samples were also performed on the field blank filters to assess possible contamination during filter deployment
170 or sample handling.

171 2.2) Sample analysis

172 Filter stages 1 to 4 were extracted using ultra-clean deionised water (DI; 18.2 M Ω) under a laminar flow cabinet (Air Science).
173 The extraction ratio was approximately 30 cm² of filter in 25 mL of DI. Extracts were immediately sonicated for one hour and
174 then stored at 4°C for at least 12 hours. Thereafter, extracts were filtered (0.2 μm) using an acid washed syringe into a clean
175 30 mL HDPE bottle and stored at -20°C until analysis (Baker et al., 2010).

176 Aerosol nitrate concentrations ($[\text{NO}_3^-]$) were determined using a Thermo Scientific Dionex Aquion Ion Chromatography
177 (IC) system (precision of $\pm 0.3 \mu\text{mol L}^{-1}$). The anion IC contained an AG22 RFIC 4 x 50 mm guard column and AG22 RFIC
178 4 x 250 mm analytical column. A six-point standard curve that encompassed the range of sample concentrations (extract $[\text{NO}_3^-]$
179]: 1.3 to 27.7 $\mu\text{mol L}^{-1}$) was run on each day of analysis (Dionex Seven Anion-II Standard) and an R^2 value > 0.999 was
180 required for sample analysis to proceed. Final aerosol $[\text{NO}_3^-]$ were corrected by subtracting the field blanks, which represented
181 35% of the total $[\text{NO}_3^-]$ on average. Aerosol samples were also analysed for $[\text{NO}_3^-]$ using a Lachat QuikChem® flow injection
182 autoanalyzer (precision of $\pm 0.8 \mu\text{mol L}^{-1}$). The average $[\text{NO}_3^-]$ measured using the Lachat QuikChem® flow injection
183 autoanalyzer and the IC system is reported (Table S3).

184 Nitrogen and oxygen isotopic ratios were measured using the denitrifier method (Sigman et al., 2001 and Casciotti et al.,
185 2002). To determine the $^{15}\text{N}/^{14}\text{N}$ and $^{18}\text{O}/^{16}\text{O}$ of NO_3^- , a natural strain of denitrifying bacteria, *Pseudomonas aureofaciens*, that
186 lack the terminal nitrous oxide (N_2O) reductase enzyme were used to convert aqueous NO_3^- quantitatively to N_2O gas. The
187 product N_2O was analysed by continuous flow isotope ratio mass spectrometry (IRMS) using a Delta V Advantage IRMS
188 interfaced with an online N_2O extraction and purification system. Individual analyses were referenced to injections of N_2O
189 from a pure gas cylinder and then standardized through comparison to the international reference materials of IAEA-N3 and
190 USGS34 for $\delta^{15}\text{N}-\text{NO}_3^-$, and IAEA-N3, USGS34 and USGS35 for $\delta^{18}\text{O}-\text{NO}_3^-$ (Table S2) (Böhlke et al., 2003). The $^{15}\text{N}/^{14}\text{N}$ of
191 samples was corrected for the contribution of ^{17}O to the peak at mass 45 using an average reported $\Delta^{17}\text{O}$ value of 26‰ from
192 atmospheric nitrate collected in the Weddell Sea (Morin et al., 2009). The pooled standard deviation for all measurements of

193 IAEA-N3 and USGS34 for $\delta^{15}\text{N-NO}_3^-$, and IAEA-N3, USGS34 and USGS35 for $\delta^{18}\text{O-NO}_3^-$ are reported (Table S2). All
194 samples were measured in triplicate in separate batch analyses. The pooled standard deviation from all replicate analyses of
195 samples was 0.25‰ for $\delta^{15}\text{N-NO}_3^-$ and 0.64‰ for $\delta^{18}\text{O-NO}_3^-$. The average $\delta^{15}\text{N-NO}_3^-$ and $\delta^{18}\text{O-NO}_3^-$ computed for each filter
196 deployment was weighted by the $[\text{NO}_3^-]$ observed for each stage and error was propagated according to standard statistical
197 practises (Table S3).

198 Seawater samples were collected in triplicate every two hours from the ship's underway system (position at depth
199 approximately 5 m) for the analysis of surface ocean nitrite concentrations ($[\text{NO}_2^-]$). $[\text{NO}_2^-]$ was analysed using the colorimetric
200 method of Grasshof et al. (1983) using a Thermo Scientific Genesys 30 visible spectrophotometer (detection limit of 0.05 μmol
201 L^{-1}) (Table S4).

202 **2.3) Air mass back trajectory analysis**

203 To determine the air mass source region for each aerosol sample, air mass back trajectories (AMBTs) were computed for each
204 hour in which the HV-AS was operational for at least 45 minutes of that hour. Given that the ship was moving, a different
205 date, time and starting location was used to compute each AMBT. An altitude of 20 m was chosen to match the height of the
206 HV-AS above sea level and 72-hour AMBTs were computed to account for the lifetime of NO_3^- in the atmosphere. All AMBTs
207 were computed with NOAA's Hybrid Single-Particle Lagrangian Integrated Trajectory model (HYSPPLIT v 4), using NCEP
208 Global Data Assimilation System (GDAS) output, which can be accessed at <https://www.arl.noaa.gov/ready/hysplit4.html>
209 (NOAA Air Resources Laboratory, Silver Spring, Maryland) (Stein et al., 2015; Rolph 2016).

210 **3) Results**

211 The coarse mode ($> 1 \mu\text{m}$ in diameter) aerosol $[\text{NO}_3^-]$ computed by summing the $[\text{NO}_3^-]$ of stages 1 through 4, ranged from
212 15.1 to 235.0 ng m^{-3} (Fig. 1a and Table 1). The mass-weighted $\delta^{15}\text{N}$ of coarse mode aerosol NO_3^- ranged from -43.1‰ to -
213 2.7‰ (Figs. 1b, 2 and Table 1). There were no clear trends in atmospheric $[\text{NO}_3^-]$ or $\delta^{15}\text{N-NO}_3^-$ with aerosol size (Table S5).

214 The highest nitrate concentrations occurred between 34° S and 45° S, and then decreased with increasing latitude. Similarly,
215 higher values characterized $\delta^{15}\text{N-NO}_3^-$ between 34° S and 45° S ($-4.9 \pm 1.3\text{‰}$), and then decreased with increasing latitude
216 (Fig. S2). At the high latitudes (south of 60° S), median values of 26.21 ng m^{-3} and -22.2‰ were observed for nitrate
217 concentration and $\delta^{15}\text{N}$, respectively. Coincident mass-weighted $\delta^{18}\text{O-NO}_3^-$ values ranged from 16.5‰ to 70‰ (Figs. 1c, 3
218 and Table 1). No latitudinal trend in $\delta^{18}\text{O-NO}_3^-$ was apparent, although distinctly low $\delta^{18}\text{O-NO}_3^-$ values were observed in the
219 Weddell Sea, as discussed in section 4.3 below. The difference between $\delta^{18}\text{O-NO}_3^-$ observed in the Weddell Sea (during
220 January to February) and $\delta^{18}\text{O-NO}_3^-$ observed at corresponding latitudes (56° S to 70° S) during the early and late summer
221 transects is statistically significant ($p\text{-value} = 0.009$). The early and late summer cruise transects were similar spatially in that
222 both took place along the same hydrographic line (i.e., the Good Hope line), apart from the deviation to South Georgia during
223 late summer (Fig. 2a & b). Even though the early and late summer cruise transects occurred in December and March,

224 respectively, there is no statistically significant difference in $[\text{NO}_3^-]$ (p-value = 0.43), $\delta^{15}\text{N-NO}_3^-$ (p-value = 0.53) or $\delta^{18}\text{O-NO}_3^-$
 225 (p-value = 0.67) between them. Therefore, the early and late summer legs are discussed together and collectively referred to
 226 as the latitudinal transect.

227

228 Table 1: The average (Avg), standard deviation (SD) and range of total coarse-mode ($> 1\mu\text{m}$) atmospheric nitrate
 229 concentration ($[\text{NO}_3^-]$; ng m^{-3}) and the mass weighted average N and O isotopic composition of coarse mode nitrate ($\delta^{15}\text{N-}$
 230 NO_3^- and $\delta^{18}\text{O-NO}_3^-$; ‰) are shown. Cruise legs are denoted as follows: early summer (ES), Weddell Sea (WS) and late
 231 summer (LS).

Leg	$[\text{NO}_3^-]$ (ng m^{-3})		$\delta^{15}\text{N-NO}_3^-$ (‰ vs. N_2)		$\delta^{18}\text{O-NO}_3^-$ (‰ vs. VSMOW)	
	Avg (SD)	Range	Avg (SD)	Range	Avg (SD)	Range
ES	88.1 (70.2)	20.0 to 235.0	-19.5 (16.4)	-42.9 to -2.7	47.1 (17.8)	16.5 to 70.0
WS	29.4 (12.1)	15.1 to 59.5	-22.7 (7.2)	-38.1 to -11.6	38.4 (12.9)	18.8 to 60.3
LS	59.7 (59.4)	16.9 to 177.4	-15.0 (8.1)	-25.6 to -4.6	50.3 (6.3)	43.1 to 58.9

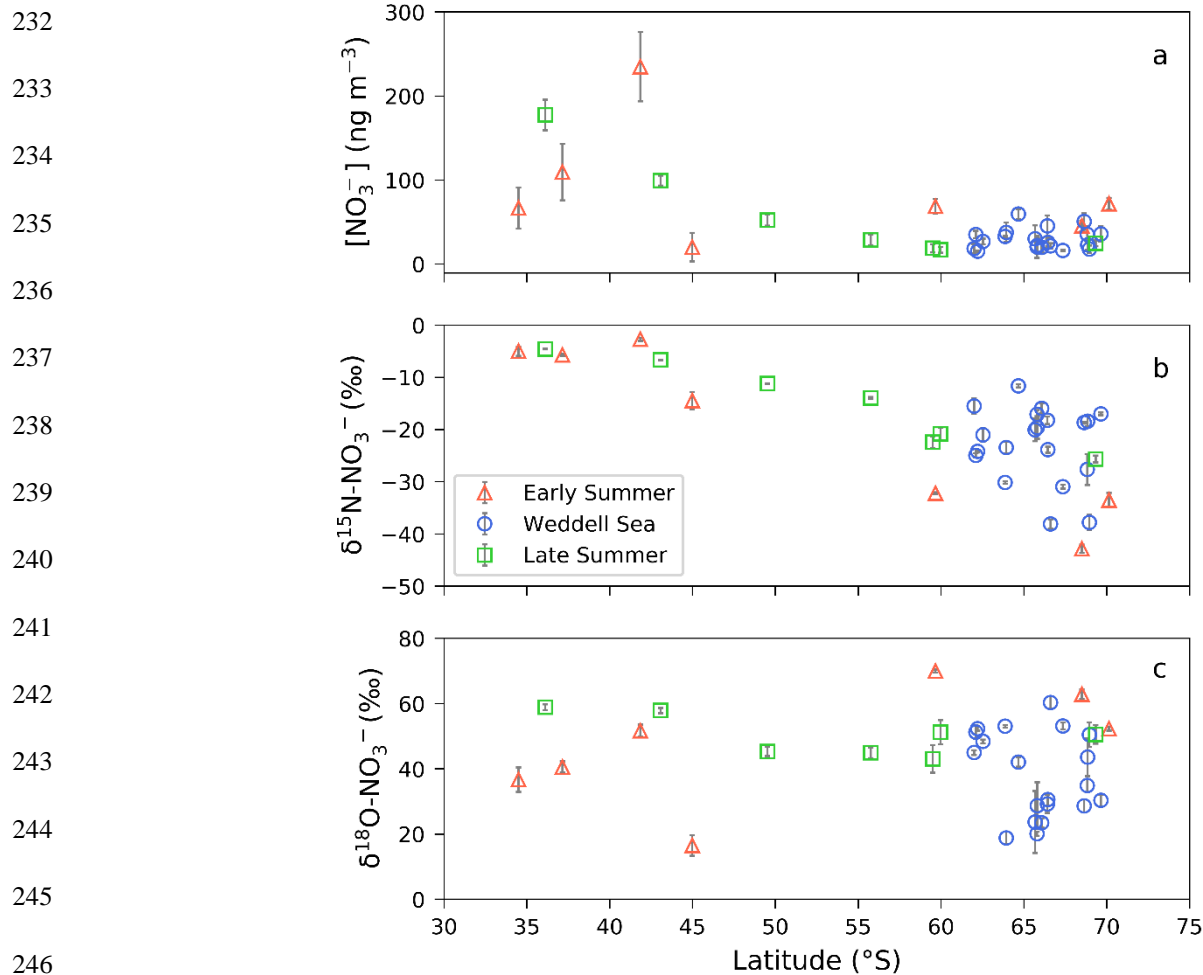
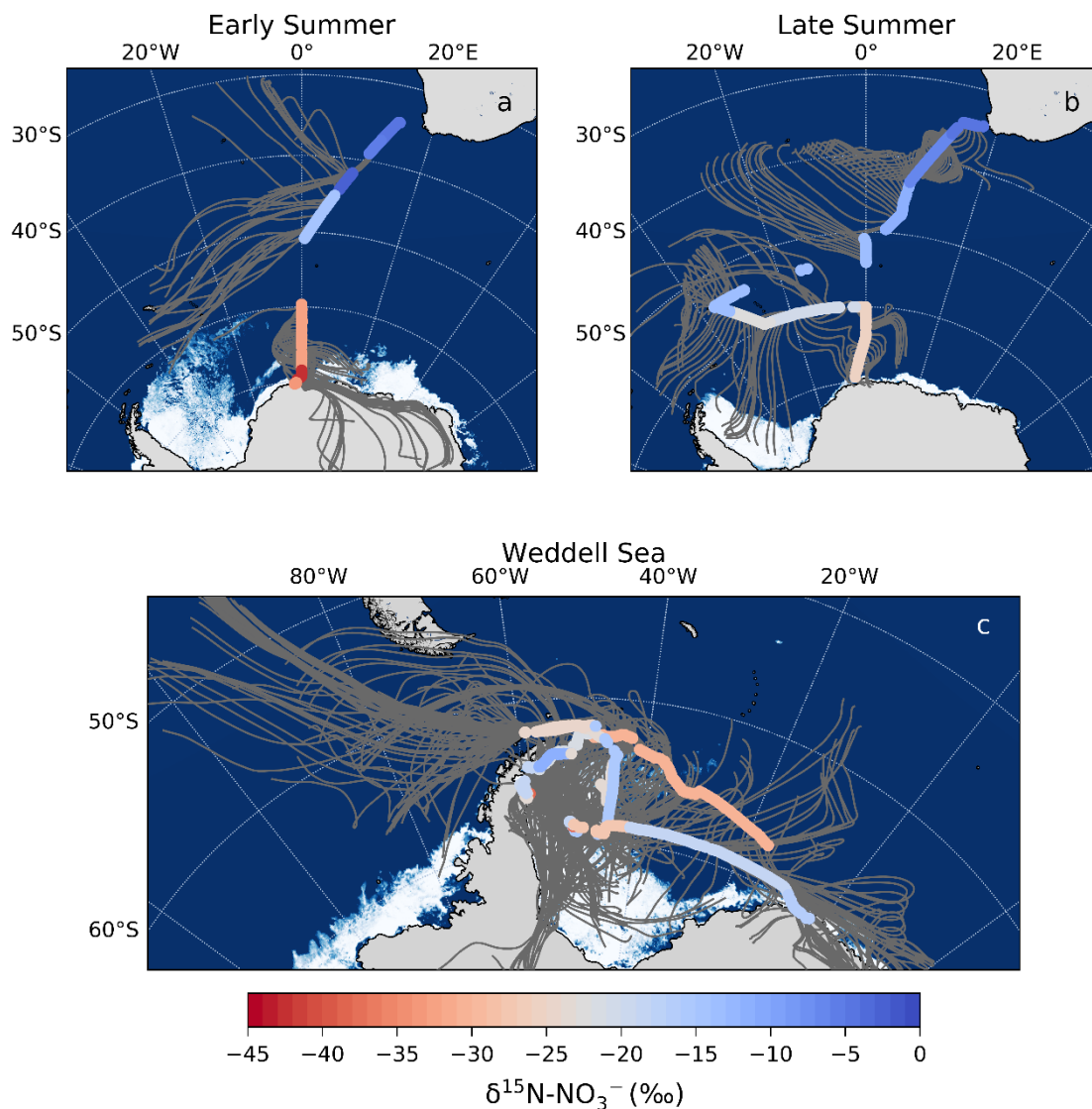


Figure 1. (a) The average (± 1 SD) coarse mode ($> 1\ \mu m$) nitrate concentration $[NO_3^-]$ ($ng\ m^{-3}$), and the weighted average (± 1 SD) $\delta^{15}N$ (b) and $\delta^{18}O$ (c) of atmospheric nitrate ($\delta^{15}N-NO_3^-$ (‰ vs. N_2) and $\delta^{18}O-NO_3^-$ (‰ vs. VSMOW), respectively), as a function of latitude (°S). Early and late summer latitudinal transects are denoted by the red triangles and green squares, respectively. Weddell Sea samples are denoted by blue circles. Where error bars (± 1 SD) are not visible, the standard deviation is smaller than the size of the marker.



270 Figure 2. 72-hour AMBTs (grey lines) computed for each hour of the voyage when the HV-AS was operational for more
 271 than 45 minutes of the hour during early summer (a), late summer (b), and in the Weddell Sea (c). The colour bar represents
 272 the weighted average $\delta^{15}\text{N}$ of coarse mode ($> 1 \mu\text{m}$) atmospheric nitrate ($\delta^{15}\text{N-NO}_3^-$). Individual AMBTs for each aerosol
 273 sample from the Weddell Sea are shown in Fig. S1. The white represents the location of the sea ice determined using satellite
 274 derived sea-ice concentration data, obtained from passive microwave sensors AMSR2 (Advanced Microwave Scanning
 275 Radiometer 2, Spreen et al., 2008).

276

277

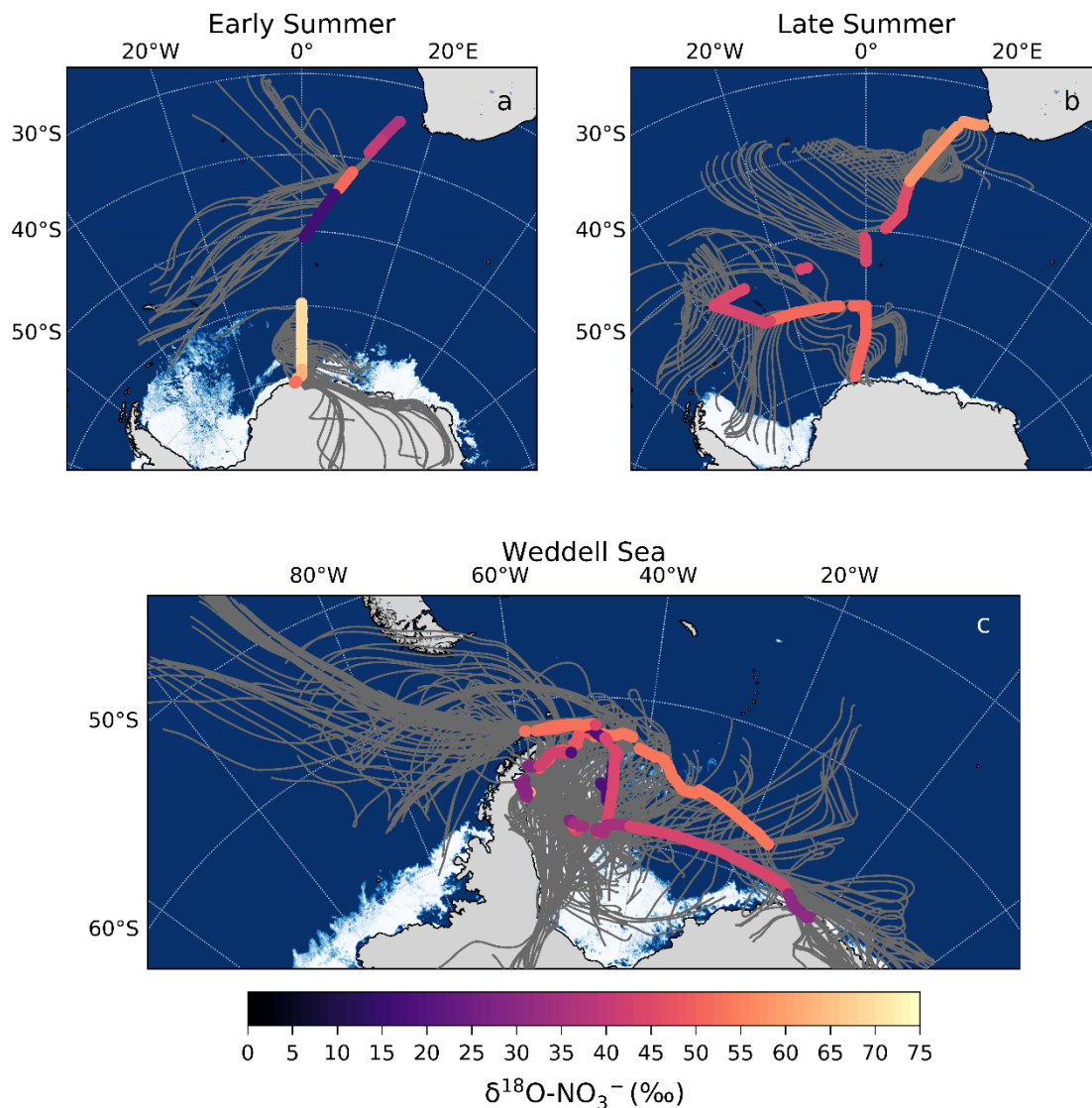


Figure. 3. 72-hour AMBTs (grey lines) computed for each hour of the voyage when the HV-AS was operational for more than 45 minutes of the hour during early summer (a), late summer (b), and in the Weddell Sea (c). The colour bar represents the weighted average $\delta^{18}\text{O}$ of coarse mode ($> 1 \mu\text{m}$) atmospheric nitrate ($\delta^{18}\text{O}\text{-NO}_3^-$). Individual AMBTs for each aerosol sample from the Weddell Sea are shown in Fig. S1. The white represents the location of the sea ice (see Fig. 2 caption).

4) Discussion

Our observations reveal a latitudinal gradient in atmospheric NO_3^- concentration and $\delta^{15}\text{N}\text{-NO}_3^-$, which we hypothesize may be attributed to the varying contribution of the dominant NO_x sources present between Cape Town and coastal Antarctica. In contrast, $\delta^{18}\text{O}\text{-NO}_3^-$ depicts no latitudinal trend; however, relatively low $\delta^{18}\text{O}\text{-NO}_3^-$ values are observed in the Weddell Sea,

300 which we hypothesize may be attributed to the influence of sea ice emissions on NO_x cycling. Below, we first discuss the
301 extent to which anthropogenic NO_x sources may influence the observed atmospheric NO₃⁻ concentrations and δ¹⁵N signatures.
302 Then we discuss the dominant NO_x sources to low, mid and high latitude Southern Ocean MBL NO₃⁻, determined in part from
303 72-hour AMBTs, as well as the role of various oxidants in NO/NO₂ cycling and NO₂ oxidation.

304 **4.1) Minimal influence of anthropogenic NO_x sources**

305 Aerosol NO₃⁻ concentrations were low (< 100 ng m⁻³; Fig. 1a) for most air masses sampled along the latitudinal transect
306 and in the Weddell Sea, consistent with the expectation of minimal influence from anthropogenic NO_x sources. For
307 comparison, [NO₃⁻] in a polluted urban airshed over South Africa can be > 500 ng m⁻³ (Collett et al., 2010). Interestingly, NO₃⁻
308 concentrations were higher (± 200 ng m⁻³; Fig. 1a) in samples collected near the South African coast at the beginning of the
309 latitudinal transect (i.e., above 43° S). However, 72-hour AMBTs computed for all latitudinal transect samples indicate that
310 sampled air masses originated from over the South Atlantic sector of the Southern Ocean (Fig. 2a and 2b), with no continental
311 influence and limited opportunity for direct anthropogenic NO_x emissions to contribute to aerosol NO₃⁻, assuming NO₃⁻ has a
312 lifetime of 72 hours (Alexander et al., 2020). Furthermore, contamination from ship stack emissions was avoided by using a
313 sector collector to restrict HV-AS activity to certain wind directions (Sect. 2.1). As such, the higher atmospheric NO₃⁻
314 concentrations observed near South Africa are best explained by greater lightning NO_x production, which generally occurs
315 between 40° S and the ITCZ during summer (Nesbitt et al., 2000; van der A et al., 2008).

316

317 **4.2) Interpretation of natural NO_x sources using the N isotopic composition of atmospheric NO₃⁻**

318 Aerosol δ¹⁵N-NO₃⁻ ranged from -2.7‰ for low-latitude air masses to -42.9‰ for high-latitude air masses (including those
319 sampled in the Weddell Sea; Fig. 1b). As discussed in section 1.1, the δ¹⁵N-NO₃⁻ reflects the δ¹⁵N of the source NO_x plus any
320 isotopic fractionation imparted from NO/NO₂ cycling or NO_x to NO₃⁻ conversion. Similar to previous studies, we surmise that
321 NO_x equilibrium fractionation is unlikely to be relevant in our system, as NO_x concentrations are significantly lower than O₃
322 concentrations (Elliott et al., 2007; Morin et al., 2009; Walters et al., 2016; Park et al., 2018). Typical O₃ concentrations
323 observed at coastal sites in Antarctica are on the order of 20 ppbv (parts per billion by volume) (Nadzir et al., 2018), whereas
324 the sum of NO and NO₂ rarely exceeds 0.04 ppbv (Jones et al., 2000; Weller et al., 2002; Bauguitte et al., 2012). Under these
325 conditions NO_x isotopic exchange occurs at a much slower rate than (R1) and (R2), such that little to no equilibrium isotope
326 fractionation is expressed and the δ¹⁵N of the NO₃⁻ should reflect the δ¹⁵N of the NO_x source (Walters et al., 2016).
327 Additionally, equilibrium isotope effects are temperature dependent (increasing with decreasing temperature) and here ambient
328 temperatures decline with increasing latitude. Therefore, if equilibrium isotope fractionation were occurring during NO-NO₂
329 cycling and/or NO_x to NO₃⁻ conversion, one would expect δ¹⁵N-NO₃⁻ to increase with latitude, as both fractionation processes
330 produce NO₃⁻ with a δ¹⁵N signature higher than the source NO_x. However, the opposite trend is observed here whereby δ¹⁵N-

331 NO_3^- decreases with increasing latitude (Fig. 1b). Therefore, we discount the hypothesis that equilibrium isotope effects can
332 explain the latitudinal gradient in $\delta^{15}\text{N-NO}_3^-$.

333 NO_3^- in the Antarctic troposphere may also derive from stratospheric denitrification, whereby HNO_3 is injected into the
334 troposphere from the stratosphere via the subsidence and penetration of polar stratospheric clouds (PSC). However, this
335 phenomenon typically occurs in winter when the tropospheric barrier is weak and the lower stratosphere is cold enough for
336 PSC formation (Savarino et al., 2007; Walters et al., 2019). Furthermore, $\delta^{15}\text{N-NO}_3^-$ originating from stratospheric inputs is
337 estimated to be $19\% \pm 3\%$ (Savarino et al., 2007), a value substantially greater than the atmospheric $\delta^{15}\text{N-NO}_3^-$ observed here
338 for high-latitude air masses; thus, we discount a direct influence from stratospheric NO_x . We propose that the observed
339 variation in atmospheric $\delta^{15}\text{N-NO}_3^-$ across the Southern Ocean is best explained by the changing contribution of three
340 dominant NO_x sources: lightning, surface ocean alkyl nitrate emissions, and photochemical production on snow and ice,
341 determined using AMBT analyses and typical NO_x source signatures where possible, as discussed below.

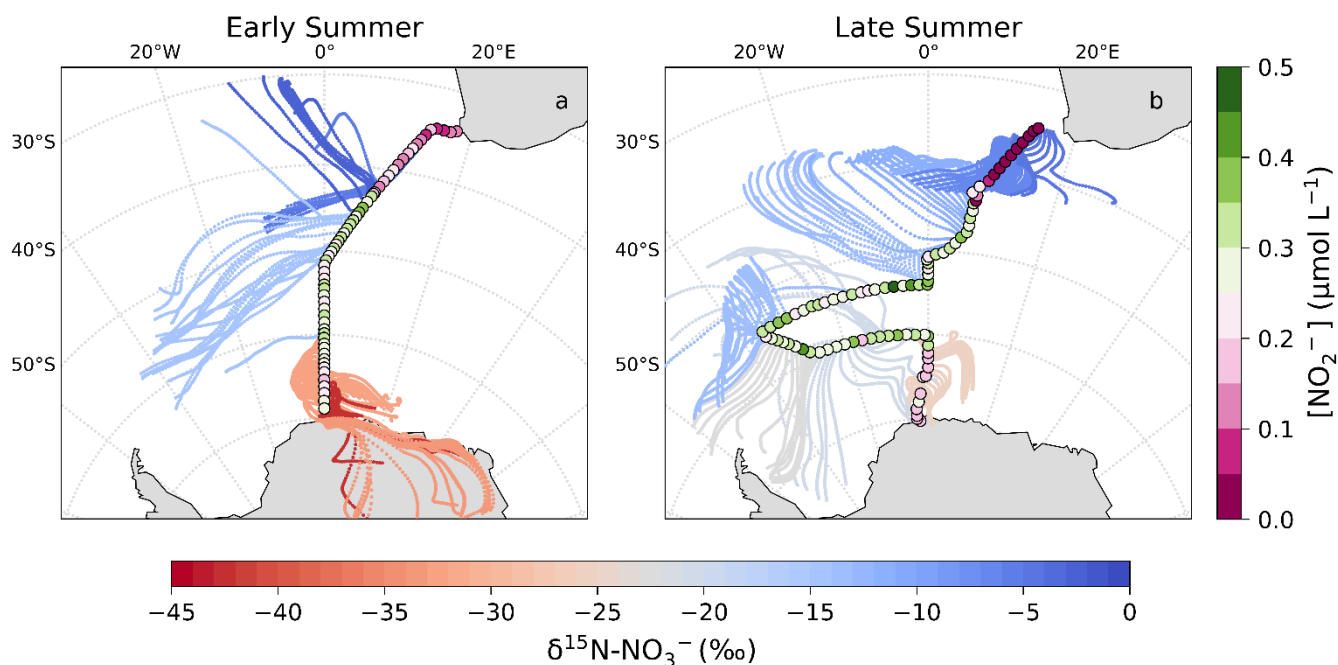
342 **4.2.1) High-latitudes: Photochemical NO_x source**

343 Aerosol $\delta^{15}\text{N-NO}_3^-$ was relatively low in air masses from the southern high-latitudes, including in the Weddell Sea (average
344 of -24.3% ; Figs. 1b & 2). The latitudinal gradient in lightning NO_x production suggests that lightning NO_x is greatly reduced
345 at high latitudes (Nesbitt et al., 2000). Similar to other studies in the region (Savarino et al., 2007; Morin et al., 2009), we
346 suggest that photochemical NO_x production on snow or ice accounts for the low aerosol $\delta^{15}\text{N-NO}_3^-$ in high-latitude air masses,
347 where high-latitude air mass samples are defined as those exposed to the Antarctic continent or the surrounding sea ice (with
348 sea ice concentration being at least 50%). Antarctic estimates for isotopic fractionation associated with snow NO_3^- photolysis
349 during summer range from -47.9% to -55.8% for laboratory and field experiments, respectively (Berhanu et al., 2014, 2015),
350 resulting in the emission of low $\delta^{15}\text{N}$ NO_x to the overlying atmosphere (Savarino et al., 2007; Morin et al., 2009; Shi et al.,
351 2018; Walters et al., 2019). Therefore, NO_3^- photolysis explains the very low $\delta^{15}\text{N-NO}_3^-$ observed in high-latitude air masses
352 in early and late summer that crossed snow-covered continental ice or sea ice before being sampled (Figs. 2a & b). During
353 early summer, air masses spent significantly more time over the snow-covered continent compared to late summer and the sea
354 ice extent was greater in early summer compared to late summer (Figs. 2a & b). Combined, these dynamics resulted in a much
355 lower $\delta^{15}\text{N-NO}_3^-$ for high-latitude air masses during early summer compared to late summer (minimum value of -42.9% vs $-$
356 25.6%). Similarly low MBL $\delta^{15}\text{N-NO}_3^-$ values ($< -30\%$) were recently observed for the southern high latitudes of the Indian
357 ocean (Shi et al., 2021). Our data are also consistent with year-round studies of atmospheric NO_3^- at coastal Antarctica
358 (Savarino et al., 2007) and the South Pole (Walters et al., 2019), where $\delta^{15}\text{N-NO}_3^-$ was reported to range from -46.9% to 10.8%
359 and from -60.8% to 10.5% , respectively. Both studies observed a seasonal cycle in $\delta^{15}\text{N-NO}_3^-$ whereby the lowest values
360 occurred during sunlit periods (i.e., summer) due to snowpack NO_x emissions and the highest values occurred during dark
361 periods (i.e., winter) due to stratospheric inputs (Savarino et al., 2007; Walters et al., 2019).

362 **4.2.2) Low- to Mid-latitudes: Oceanic NO_x source**

363 At the northern extent of our transects, the low-latitude aerosol samples, defined as those with air mass back trajectories
364 originating from anywhere north of 43° S in early summer and 41° S in late summer (Fig. 2), had the highest average $\delta^{15}\text{N-NO}_3^-$
365 NO_3^- signature ($-4.9 \pm 1.3\text{‰}$; $n = 5$). These values can be attributed to lightning-generated NO_x, which has a $\delta^{15}\text{N}$ signature
366 close to 0‰ (Hoering 1957). Lightning activity at the low latitudes is also consistent with the higher atmospheric $[\text{NO}_3^-]$
367 observed (Fig. 1a) and is further supported by co-occurring high $[\text{NO}_3^-]$ and relatively high $\delta^{15}\text{N-NO}_3^-$ (Fig. S2). An average
368 atmospheric $\delta^{15}\text{N-NO}_3^-$ signature of -4‰ was previously reported for the low latitude Atlantic Ocean, between 45° S and 45°
369 N, and similarly attributed to a combination of natural NO_x sources including lightning (Morin et al., 2009).

370 Aerosol samples across the mid-latitudes had an average $\delta^{15}\text{N-NO}_3^-$ of -13.2‰ (Figs. 1b & 2). Mid-latitude air masses are
371 defined as those originating from anywhere south of 43° S in early summer and south of 41° S in late summer that made no
372 contact with Antarctica or any surrounding sea ice (Fig. 2a & b), therefore these samples were unlikely to be influenced by
373 snow emitted NO_x with its light isotopic signature. The beginning of the mid-latitude zone (i.e., 43°S and 41°S in early and
374 late summer, respectively) was defined by the presence of non-zero sea surface nitrite concentrations in early and late summer
375 (Fig. 4). However, the observed aerosol $\delta^{15}\text{N-NO}_3^-$ was too low (-14.5‰ to -11.2‰) to be explained solely by lightning
376 generated NO_x. In the absence of any signature of anthropogenic NO_x emissions (Sect. 4.1), we argue that the dominant NO_x
377 source for the mid-latitude samples originates from seawater.



378 Figure 4. 72-hour AMBTs computed for each hour of the voyage during early (a) and late (b) summer, when the HV-AS
 379 was operational for more than 45 minutes of the hour. AMBTs are colour coded by the weighted average $\delta^{15}\text{N}$ of atmospheric
 380 nitrate ($\delta^{15}\text{N-NO}_3^-$), represented by the horizontal colour bar. Over-layered are the surface ocean nitrite concentrations (circles;
 381 $[\text{NO}_2^-]$; $\mu\text{mol L}^{-1}$), measured along each transect and represented by the vertical colour bar.

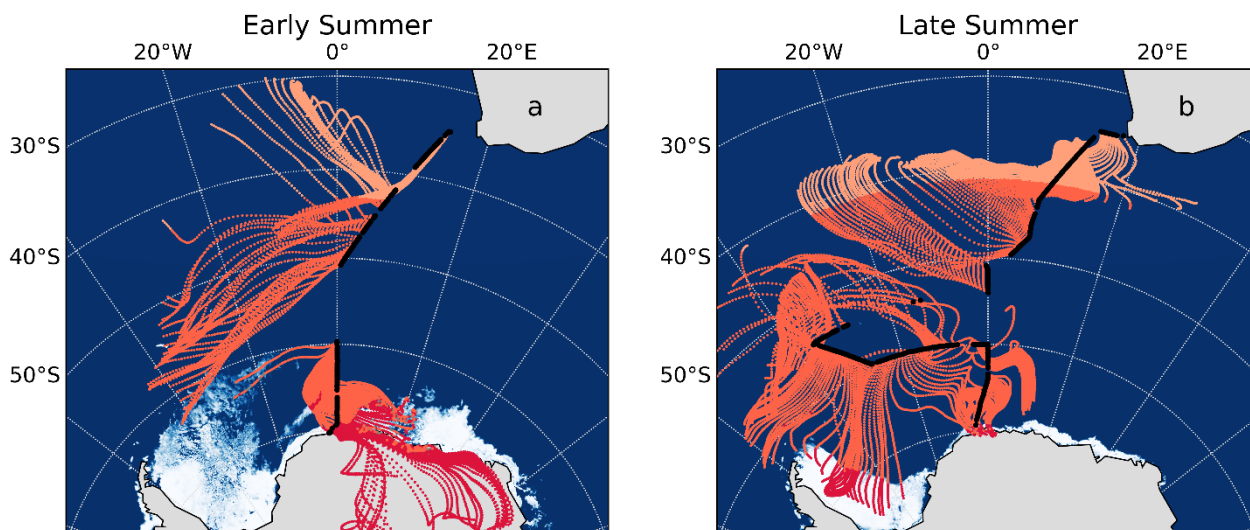
382

383 As mentioned in section 1, the most likely mechanism for an oceanic NO_x source is via the photolysis of surface ocean
 384 derived RONO_2 in the MBL. NO derived from seawater nitrite is thought to limit RONO_2 production (Dahl and Saltzman
 385 2008; Dahl et al., 2012), such that non-zero nitrite concentrations are required for RONO_2 production to occur. Here, surface
 386 ocean nitrite concentrations were relatively high, in particular from $\sim 41^\circ\text{S}$ to 50°S (Fig. 4). Furthermore, the latitudinal
 387 extent of mid-latitude air masses with low $\delta^{15}\text{N-NO}_3^-$ signatures corresponds well with the same latitudinal extent in which
 388 non-zero surface ocean nitrite concentrations occurred (Fig. 4). As such, we suggest that in this region oceanic RONO_2
 389 emission is the main source to the Southern Ocean MBL, ultimately resulting in the low $\delta^{15}\text{N-NO}_3^-$ values observed for mid-
 390 latitude air masses.

391 No estimates exist for the $\delta^{15}\text{N}$ of oceanic RONO_2 , however RONO_2 photolysis may yield isotopically light NO_x given that
 392 NO_3^- photolysis produces low $\delta^{15}\text{N}$ products (e.g., Frey et al., 2009). Therefore, once oxidised in the overlying atmosphere,
 393 NO_x derived from oceanic RONO_2 photolysis may form atmospheric NO_3^- with a low $\delta^{15}\text{N}$ signature. Aerosol $\delta^{15}\text{N-NO}_3^-$

394 values have been observed to range from -14.1‰ to -7.3‰ in the eastern equatorial Pacific (Kamezaki et al., 2019) and from
395 -6‰ to ~0‰ (average = -3.4‰) in the western equatorial Pacific (Shi et al., 2021). Observed $\delta^{15}\text{N-NO}_3^-$ is higher in the
396 western compared the eastern equatorial Pacific, which could be attributed to the proximity of the western equatorial Pacific
397 to continental/anthropogenic NO_x sources, resulting in NO_3^- having a higher $\delta^{15}\text{N}$ signature. The low average $\delta^{15}\text{N-NO}_3^-$
398 observed for the mid-latitude air masses of the Southern Ocean MBL sampled in the present study (-14.5‰ to -11.2‰), are
399 remarkably similar to those observed in the eastern equatorial Pacific (Kamazaki et al., 2019). Kamezaki et al., (2019) also
400 concluded that such low $\delta^{15}\text{N-NO}_3^-$ values cannot be explained solely by lightning NO_x and given the lack of considerable
401 influence from any continental NO_x sources, they invoked the contribution of oceanic N emissions in the form of ammonia
402 (NH_3) and/or RONO_2 . However, NH_3 flux data for the summertime Atlantic Southern Ocean derived from in situ
403 ocean/atmosphere observations suggest that the ocean in this region is a net sink of NH_3 (Altieri et al., 2021).

404 The latitudinal extent of our sampling campaign enabled us to estimate a range of likely values for the N isotopic
405 composition of NO_3^- derived from oceanic RONO_2 . We split the latitudinal transect into three regions, each characterised by
406 the dominance of a different natural source of NO_3^- , i.e., lightning NO_x at the low-latitudes (Fig. 5 light orange), oceanic
407 RONO_2 emissions at the mid-latitudes (Fig. 5 dark orange) and snowpack emissions at the high-latitudes (Fig. 5 red).



408 Figure 5. 72-hour AMBTs computed for each hour of the voyage during early (a) and late (b) summer, when the HV-AS
409 was operational for more than 45 minutes of the hour. Light orange, dark orange and red AMBTs represent time spent over
410 the low, mid- and high latitude SO, respectively. The white represents the location of the sea ice (see Fig. 2 caption).

411
412 Assuming that the dominant natural source of NO_3^- is the only source relevant in each latitudinal zone, we estimate the
413 contribution of each source to total NO_3^- formation by ascertaining the amount of time air masses spent in each zone. We
414 further assume that atmospheric $\delta^{15}\text{N-NO}_3^-$ reflects at most a combination of two sources based on the AMBTs of each sample,
415 either lightning NO_x and oceanic RONO_2 emissions near South Africa, or oceanic RONO_2 emissions and snowpack NO_x

416 emissions near Antarctica (Fig. 5 and Table S6). Using a two-end member mixing model the $\delta^{15}\text{N}$ signature of the source NO_3^-
417 derived from mid-latitude Southern Ocean RONO_2 emissions was calculated for all samples where air masses from the mid-
418 latitude region contributed at least 10% (Table S6). This 10% threshold was chosen as the isotopic endmember of oceanic
419 RONO_2 is harder to determine with confidence when its contribution to total NO_3^- is less than 10%. As an example, the
420 AMBTs for sample ES 4 spent 3% of the time in the low-latitude zone and 97% in the mid-latitude zone. Using the measured
421 $\delta^{15}\text{N-NO}_3^-$ for ES 4 of -14.5‰ and assuming lightning NO_x has a $\delta^{15}\text{N}$ signature of 0‰, we calculate the $\delta^{15}\text{N}$ signature of the
422 RONO_2 -derived NO_3^- to be -14.9‰. It is important to note that using this approach to estimate the $\delta^{15}\text{N-NO}_3^-$ from oceanic
423 RONO_2 emissions relies heavily on AMBTs generated using HYSPLIT. While HYSPLIT is a frequently used tool for assessing
424 air mass origin in the Southern Hemisphere and over Antarctica (Morin et al., 2008; Walters et al., 2019; Shi et al., 2021), it is
425 important to note that a spatial uncertainty of 15% to 30% of the trajectory path distance can be expected (Scarchilli et al.,
426 2011). AMBTs also become increasingly uncertain the further back in time they are used (Sinclair et al., 2013). Some of this
427 uncertainty is alleviated by the fact that the AMBTs generated here are relatively short (< 5 days). Additionally, the spatial
428 scale of the low-, mid- and high-latitude zones is large, such that some variation in sample AMBTs will not significantly alter
429 the expected dominant NO_3^- source.

430 Using this approach for each filter deployment along the latitudinal transect, an average $\delta^{15}\text{N-NO}_3^-$ from oceanic RONO_2
431 emissions of $-21.8 \pm 7.6\text{‰}$ was estimated. Furthermore, the contribution of RONO_2 emissions can explain the lowering of
432 $\delta^{15}\text{N}$ from 0‰ for the low-latitude air mass samples. For example, the highest $\delta^{15}\text{N}$ observed in the study was -2.7‰, and this
433 sample has a < 5% contribution from the mid-latitude zone. The other two low-latitude samples have 30% to 40% contribution
434 from the mid-latitude zone and their $\delta^{15}\text{N}$ is lower (Table S3), as expected due to the influence of RONO_2 emissions.

435 The influence of low $\delta^{15}\text{N-NO}_3^-$ from RONO_2 emissions is not limited to the Southern Ocean, and this estimate of the N
436 isotopic composition for the RONO_2 derived NO_3^- source may be useful to constrain the contribution of RONO_2 emissions to
437 NO_3^- formation in other ocean regions with elevated surface ocean nitrite concentrations, such as the tropical Pacific.

438 4.3) The O isotopes of atmospheric nitrate

439 The corresponding $\delta^{18}\text{O}$ values allow us to determine the pathways of NO_3^- formation from NO_x . However, an assumption
440 must first be made regarding the oxidation of NO to NO_2 . While the dominant oxidant of NO to NO_2 is O_3 (R1) in most of the
441 troposphere, over the open ocean there can be a significant contribution via the reaction of NO with peroxy radicals (HO_2 and
442 its organic homologues RO_2) (Alexander et al., 2020). Peroxy radicals compete with O_3 to convert NO into NO_2 via R10:



444 The $\delta^{18}\text{O}$ of peroxy radicals is much lower than that of O_3 because the O atoms derive from atmospheric O_2 , which has a well-
445 defined $\delta^{18}\text{O}$ of 23.9‰ (Kroopnick and Craig, 1972). The $\delta^{18}\text{O-NO}_2$ can then be calculated using Eq. (2),

$$446 \delta^{18}\text{O-NO}_2 = (\delta^{18}\text{O-O}_2)(1-f) + (\delta^{18}\text{O-O}_3^*)(f) \quad (2)$$

447 where f is the fraction of NO_2 formed from R1, (1-f) is the fraction formed from R10, and the terminal $\delta^{18}\text{O-O}_3$ value ($\delta^{18}\text{O-}$
448 O_3^*) is $130.4 \pm 12.9\text{‰}$ (Vicars and Savarino, 2014).

449 The $\delta^{18}\text{O}-\text{NO}_3^-$ is then determined using Eq. (3) in which two thirds of the O atoms in NO_3^- come from NO_2 and one third
450 comes from OH i.e., R3, or using Eq. (4) in which three sixths of the O atoms in NO_3^- come from O_3 , two sixths come from
451 NO_2 and one sixth comes from H_2O i.e., R4-R6 (Hastings et al., 2003; Alexander et al., 2020).

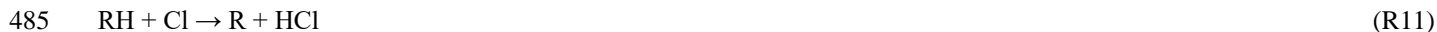
$$452 \delta^{18}\text{O}-\text{NO}_3^-(\text{R3}) = (2/3)(\delta^{18}\text{O}-\text{NO}_2) + (1/3)(\delta^{18}\text{O}-\text{OH}) \quad (3)$$

$$453 \delta^{18}\text{O}-\text{NO}_3^-(\text{R4-R6}) = (1/2)(\delta^{18}\text{O}-\text{O}_3^*) + (1/3)(\delta^{18}\text{O}-\text{NO}_2) + (1/6)(\delta^{18}\text{O}-\text{H}_2\text{O}) \quad (4)$$

454 We assume that 15% of NO to NO_2 conversion occurs via HO_2/RO_2 oxidation and 85% by O_3 oxidation as is suggested by
455 global models (Alexander et al., 2020), and use the minimum and maximum $\delta^{18}\text{O}-\text{H}_2\text{O}$ range of -27.5‰ to 0‰, the
456 temperature-dependent equilibrium isotope exchange between OH and H_2O (Walters and Michalski, 2016), and the resulting
457 minimum and maximum estimates for $\delta^{18}\text{O}-\text{OH}$ of -67.4‰ to -41.0‰. Using these assumptions and Eq. (3) and (4), the
458 expected $\delta^{18}\text{O}-\text{NO}_3^-$ for the daytime OH oxidation pathway (R3) is 46.5‰ to 71.4‰, and for the dark reactions (R4-R6) is
459 88.7‰ to 113.5‰. The observed $\delta^{18}\text{O}-\text{NO}_3^-$ values were all less than 70‰ (Figs. 1c and 3), suggesting that NO_x oxidation by
460 OH (R3) was indeed the dominant pathway for atmospheric NO_3^- formation during summer. The low $\delta^{18}\text{O}-\text{NO}_3^-$ values
461 observed suggest a minimal influence of O_3 in the oxidation chemistry, ruling out both the halogen (R8 to R9) and DMS (R7)
462 related NO_3^- formation pathways in addition to N_2O_5 hydrolysis (R4-6). This is consistent with previous year-round studies of
463 atmospheric NO_3^- at coastal Antarctica (Savarino et al., 2007) and the South Pole (Walters et al., 2019) where $\delta^{18}\text{O}-\text{NO}_3^-$ was
464 at a minimum in summer (59.6‰ and 47.0‰, respectively). Both studies confirm the importance of HO_x oxidation chemistry
465 in summer when solar radiation enhances the production of these oxidants, followed by a switch to O_3 dominated oxidation
466 chemistry in winter (Savarino et al., 2007; Ishino et al., 2017; Walters et al., 2019).

467 Interestingly, most aerosol samples have a $\delta^{18}\text{O}-\text{NO}_3^-$ less than 46.5‰ (n=19), the lower limit estimated above for the OH
468 pathway. This suggests that there is more NO to NO_2 conversion via HO_2/RO_2 oxidation occurring than the global average. A
469 maximum HO_2/RO_2 contribution to NO oxidation of ~63% is required to explain the lowest $\delta^{18}\text{O}-\text{NO}_3^-$ value, which was
470 observed over the mid-latitudes during early summer. Increased RO_2 production over the mid-latitudes could derive from
471 RONO_2 photolysis in the MBL, which we hypothesise is happening in this region based on the $\delta^{15}\text{N}-\text{NO}_3^-$ (Sect. 4.2.2).
472 Although the lowest $\delta^{18}\text{O}$ observation occurred in the mid-latitudes, the majority of low $\delta^{18}\text{O}-\text{NO}_3^-$ values were observed in
473 the Weddell Sea, away from the region of maximum RONO_2 emissions. Approximately half of the Weddell Sea samples have
474 a $\delta^{18}\text{O}-\text{NO}_3^- < 31\%$, which would require a HO_2/RO_2 contribution to NO oxidation upwards of 40% (more than double the
475 contribution estimated by global models (Alexander et al., 2020)). These $\delta^{18}\text{O}-\text{NO}_3^-$ observations are unusually low compared
476 to previous observations for the same region in spring (Morin et al., 2009). We hypothesize that the large contribution of
477 HO_2/RO_2 to NO/ NO_2 oxidation (i.e., a decrease in f in Eq. (2)) resulting in these low $\delta^{18}\text{O}-\text{NO}_3^-$ values is due to the influence
478 of sea ice emissions. The 72-hour AMBTs for these low $\delta^{18}\text{O}-\text{NO}_3^-$ Weddell Sea samples indicate that all the air masses either
479 originated from, or spent a significant amount of time recirculating, over the sea ice covered region of the western Weddell
480 Sea (Fig. 6b). By contrast, aerosol samples from the Weddell Sea with $\delta^{18}\text{O}-\text{NO}_3^-$ values greater than 31‰ have air masses
481 that experienced significantly more oceanic influence (Fig. 6a). There is evidence that sea ice can lead to enhanced peroxy
482 radical production (Brough et al., 2019). In that work, increased $\text{HO}_2 + \text{RO}_2$ concentrations were observed during spring at a

483 coastal Antarctic site when air masses arrived from across a sea ice covered zone. This was attributed to the oxidation of
484 hydrocarbons by chlorine atoms, which leads to increased RO_2 concentrations via R11 and R12:



487

488

489

490

491

492

493

494

495

496

497

498

499

500

501

502

503

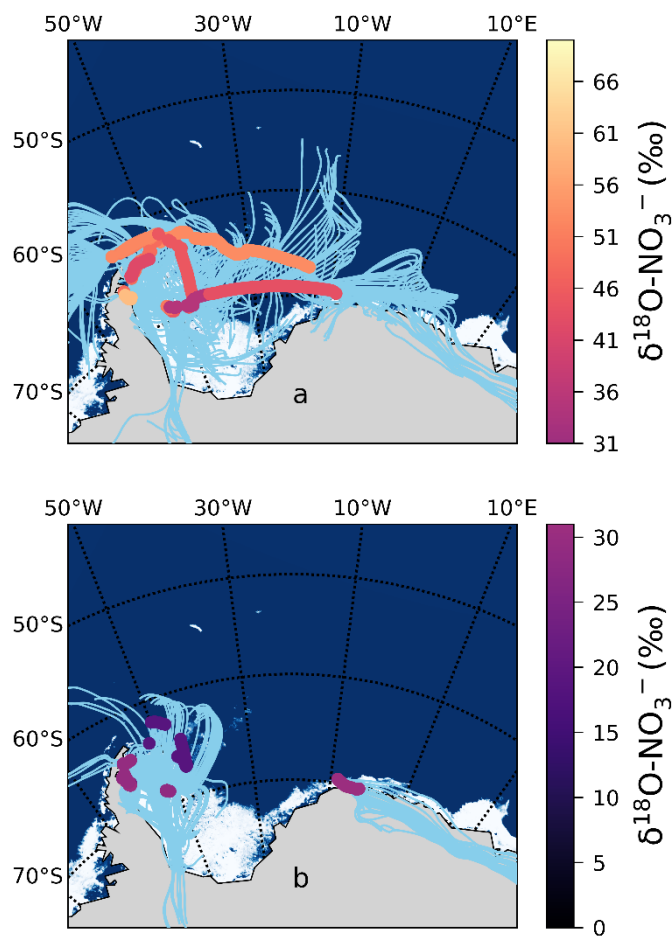
504

505

506

507

508



509 Figure. 6. 72-hour AMBTs (light blue lines) computed for each hour of the voyage in the Weddell Sea, when the HV-AS
510 was operational for more than 45 minutes of the hour. The vertical colour bar represents the weighted average $\delta^{18}\text{O}$ of
511 atmospheric nitrate ($\delta^{18}\text{O}-\text{NO}_3^-$), where $\delta^{18}\text{O}-\text{NO}_3^-$ was $> 31\text{‰}$ (a) and $< 31\text{‰}$ (b). The white represents the location of the sea
512 ice (see Fig. 2 caption).

513

514 Cl atoms are much more reactive with hydrocarbons than OH (Monks, 2005) and can enhance hydrocarbon oxidation even
515 when present at low concentrations. Brough et al. (2019) suggest that air masses that traversed the sea ice zone contained
516 photolabile chlorine compounds that built up at night until photolysis occurred during the next day (Brough et al., 2019).

517 Although our study was conducted in summer (the season of minimum sea ice extent), the sampling locations were uniquely
518 positioned at the western edge of the Weddell Sea gyre where significant sea ice remained (Fig. 6). Therefore, we suggest that
519 chlorine chemistry over the sea ice increased RO₂ concentrations at the time of our sampling, allowing the NO + RO₂ pathway
520 to play a more significant role in the Weddell Sea and resulting in low δ¹⁸O-NO₃⁻ values. We note that the only other estimates
521 of δ¹⁸O-NO₃⁻ from the Weddell Sea ranged from ~ 50‰ to 110‰ during springtime, and these samples were associated with
522 air masses that spent almost no time over the sea ice and therefore had limited potential for this peroxy radical chemistry to
523 drive down the δ¹⁸O-NO₃⁻ to the low values we observe (Morin et al., 2009).

524 **5) Conclusions**

525 Our observations across a large latitudinal gradient of the summertime Southern Ocean MBL suggest it is dominated by natural
526 NO_x sources with distinct isotopic signatures. Aerosol NO₃⁻ was predominantly formed from lightning generated NO_x with a
527 δ¹⁵N of ~ 0‰ at the lower latitudes, whereas snowpack NO_x emissions with a δ¹⁵N ~ -48‰ dominated the MBL inventory at
528 higher latitudes. Over the mid-latitudes, NO₃⁻ derived primarily from oceanic RONO₂ emissions, with an estimated δ¹⁵N
529 signature of ~ -22.0‰. Additional research is needed to improve our mechanistic and isotopic understanding of surface ocean
530 RONO₂ formation, flux, and conversion to aerosol nitrate in order to constrain the contribution of oceanic RONO₂ emissions
531 to NO₃⁻ formation in other ocean regions where this source has been invoked, such as the tropical Pacific (Kamezaki et al.,
532 2019). The isotopic composition of NO₃⁻ observed here can further inform interpretations of Antarctic ice core NO₃⁻ isotope
533 records to understand aerosol climate forcing and controls on the atmospheric oxidation budget over millennia (Freyer et al.,
534 1996; Jiang et al., 2019) – the interpretation of which relies on knowledge of the NO_x isotopic source signatures in the polar
535 atmosphere.

536 The δ¹⁸O-NO₃⁻ values were consistently lower than 70‰, which confirms NO_x oxidation by OH (R3) to be the dominant
537 pathway for atmospheric NO₃⁻ formation during summer. However, unusually low δ¹⁸O-NO₃⁻ values observed at the mid-
538 latitudes and in the Weddell Sea indicate the increased importance of peroxy radicals (and decreased importance of O₃) in NO
539 oxidation to NO₂ in the MBL. At the mid latitudes peroxy radicals (RO₂) may derive from RONO₂ photolysis, while in the
540 Weddell Sea, sea ice appears to play an important role in the formation of this oxidant via its influence on chlorine chemistry
541 (Brough et al., 2019). This implies that snow covered sea ice is not only a source of NO_x but also other species that have the
542 potential to change the composition of the atmosphere above the ice and impact NO_x oxidation chemistry. These results also
543 highlight the utility of δ¹⁸O-NO₃⁻ to identify the major oxidants in NO oxidation, as well as NO_x to NO₃⁻ conversion. In
544 particular, δ¹⁸O-NO₃⁻ can serve as a useful tool for testing our understanding of the relative importance of HO₂/RO₂ in NO/NO₂
545 cycling, which can be difficult to constrain in some environments.

546 Our study challenges the traditional paradigm that considers the ocean as a passive recipient of N deposition, as the
547 Southern Ocean mid-latitude NO₃⁻ source may derive almost entirely from oceanic RONO₂ emissions. In the tropical equatorial
548 Pacific atmosphere, Kamezaki et al. (2019) also suggested evidence for a low δ¹⁵N-NO₃⁻ source derived from the ocean. In the

549 subtropical Atlantic Ocean MBL, Altieri et al. (2016) found that biogeochemical cycling in the surface ocean can directly
550 influence the lower atmosphere serving as a source of aerosol organic N and ammonium. This study suggests that the surface
551 waters of the Southern Ocean may also serve as a NO_x source, ultimately resulting in NO₃⁻ aerosol formation. As such, the
552 surface ocean may play a bigger role in atmospheric oxidative capacity over remote marine regions than previously thought.

553
554 *Author contributions.* K.E.A designed the study and sampling campaign, acquired funding and supervised the research. K.E.A
555 and J.G. provided financial and laboratory resources and assisted in data validation. K.A.M.S. and J.M.B conducted the
556 sampling at-sea and J.M.B. performed the laboratory analyses. M.G.H and E.J. assisted in data validation, reviewing, and
557 editing the manuscript. J.M.B analysed the data and prepared the manuscript with contributions from all co-authors.

558
559 *Competing interests.* The authors declare that they have no conflict of interest.

560
561 *Data availability statement.* Data sets for this research are available at <https://doi.org/10.5281/zenodo.5740618>.

562
563 *Acknowledgements.* We thank the Captain and crew of the R/V *SA Agulhas II* for their support at sea and the Marine
564 Biogeochemistry Lab in the Oceanography Department at the University of Cape Town for their assistance in the field and
565 laboratory. We thank Lija Treibergs, Reide Jacksin and Peter Ruffino for their assistance in analysing the nitrate isotopes and
566 Riesna Audh for her assistance with satellite derived sea ice concentration data. We thank Riesna Audh, Raquel Flynn and
567 Shantelle Smith for nitrite concentration measurements, and Raquel Flynn for quality controlling the nitrite concentration data.
568 This research was partially funded by a CAREER award to J.G. from the U.S. National Science Foundation (OCE-1554474).
569 This research was also supported by the South African National Research Foundation through a Competitive Support for Rated
570 Researchers Grant to K.E.A. (111716), South African National Antarctic Programme Postgraduate Fellowship to J.M.B, and
571 Grant to K.E.A (110732); UCT support to K.E.A. through a University Research Council Launching Grant and VC Future
572 Leaders 2030 Grant.

573 **6) References**

574 Alexander, B., and Mickley, L. J.: Paleo-perspectives on the potential future changes in the oxidative capacity of the
575 atmosphere due to climate change and anthropogenic emissions, *Curr Pollution Rep.*, 1, 57-69,
576 <https://doi.org/10.1007/s40726-015-0006-0>, 2015.

577 Alexander, B., Sherwen, T., Holmes, C. D., Fisher, J. A., Chen, Q., Evans, A. J., and Kasibhatla, P.: Global inorganic nitrate
578 production mechanisms: comparison of a global model with nitrate isotope observations. *Atmos. Chem. Phys.*, 20(6),
579 3859-3877, <https://doi.org/10.5194/acp-20-3859-2020>, 2020.

580 Altieri, K. E., Fawcett, S. E., and Hastings, M.G.: Reactive Nitrogen Cycling in the Atmosphere and Ocean, *Annu. Rev. oEarth*
581 *Planet. Sci.*, 49, 513-540, <https://doi.org/10.1146/annurev-earth-083120-052147>, 2021.

582 Altieri, K. E., Fawcett, S. E., Peters, A. J., Sigman, D. M., and Hastings, M. G.: Marine biogenic source of atmospheric organic
583 nitrogen in the subtropical North Atlantic, *PNAS.*, 113(4), 925-930, <https://doi.org/10.1073/pnas.1516847113>, 2016

584 Altieri, K. E., Hastings, M. G., Gobel, A. R., Peters, A. J., and Sigman, D. M.: Isotopic composition of rainwater nitrate at
585 Bermuda: the influence of air mass source and chemistry in the marine boundary layer, *J. Geophys. Res. Atmos.*, 118,
586 11304-11316, <https://doi.org/10.1002/jgrd.50829>, 2013.

587 Atlas, E., Pollock, W., Greenberg, J., Heidt, L., and Thompson, A. M.: Alkyl nitrates, nonmethane hydrocarbons, and
588 halocarbon gases over the equatorial Pacific Ocean during Saga 3, *J. Geophys. Res. Atmos.*, 98(D9), 16933-16947,
589 <https://doi.org/10.1029/93JD01005>, 1993.

590 Baker, A. R., Lesworth, T., Adams, C., Jickells, T. D., and Granzveld, L.: Estimation of atmospheric nutrient inputs to the
591 Atlantic Ocean from 50°N to 50°S based on large-scale field sampling: Fixed nitrogen and dry deposition of
592 phosphorus, *Global Biogeochem. Cycles*, 24, GB3006, <https://doi.org/10.1029/2009GB003634>, 2010.

593 Bauguitte, A. J.-B., Bloss, W. J., Evans, M. J., Salmon, R. A., Anderson, P. S., Jones, A. E., Lee, J. D., Saiz-Lopez, A., Roscoe,
594 H. K., Wolff, E. W., and Plane, J. M. C.: Summertime NO_x measurements during the CHABLIS campaign: can source
595 and sink estimates unravel observed diurnal cycles?, *Atmos. Chem. Phys.*, 12, 989-1002, [https://doi.org/10.5194/acp-](https://doi.org/10.5194/acp-12-989-2012)
596 [12-989-2012](https://doi.org/10.5194/acp-12-989-2012), 2012.

597 Behrenfeld, M. J., Boss, E., Siegel, D. A., and Shea, D. M.: Carbon-based ocean productivity and phytoplankton physiology
598 from space, *Global Biogeochem. Cycles*, 19(1), 1-14, <https://doi.org/10.1029/2004GB002299>, 2005.

599 Berhanu, T. A., Meusinger, C., Erbland, J., Jost, R., Bhattacharya, S. K., Johnson, M. S., and Savarino, J.: Laboratory study
600 of nitrate photolysis in Antarctic snow. II. Isotopic effects and wavelength dependence, *J. Chem. Phys.*, 140(244306),
601 1-14, <https://doi.org/10.1063/1.4882899>, 2014.

602 Berhanu, T. A., Savarino, J., Erbland, J., Vicars, W. C., Preunkert, S., Martins, J. F., and Johnson, M. S.: Isotopic effects of
603 nitrate photochemistry in snow: a field study at Dome C, Antarctica, *Atmos. Chem. Phys.*, 15, 11243-11256,
604 <https://doi.org/10.5194/acp-15-11243-2015>, 2015.

605 Blake, N. J., Blake, D. R., Swanson, A. L., Atlas, E., Flocke, F., and Rowland, F. S.: Latitudinal, vertical, and seasonal
606 variations of C₁-C₄ alkyl nitrate in the troposphere over the Pacific Ocean during PEM-Tropics A and B: Oceanic and
607 continental sources, *J. Geophys. Res. Atmos.*, 108(D2), 1-14, <https://doi.org/10.1029/2001JD001444>, 2003.

608 Blake, N. J., Blake, D. R., Wingenter, O. W., Sive, B. C., Kang, C. H., Thornton, D. C., Bandy, A. R., Atlas, E., Flocke, F.,
609 Harris, J. M., and Rowland, F. S.: Aircraft measurements of the latitudinal, vertical, and seasonal variations of
610 NMHCs, methyl nitrate, methyl halides, and DMS during the First Aerosol Characterization Experiment (ACE 1), *J.*
611 *Geophys. Res. Atmos.*, 104(D17), 21803-21817, <https://doi.org/10.1029/1999JD900238>, 1999.

612 Böhlke, J. K., Mroczkowski, S. J., and Coplen, T. B.: Oxygen isotopes in nitrate: new reference materials for ¹⁸O:¹⁷O:¹⁶O
613 measurements and observations on nitrate-water equilibrium, *Rapid Commun. Mass Spectrom.*, 17(16), 1835-1846,
614 <https://doi.org/10.1002/rcm.1123>, 2003.

615 Brough, N., Jones, A. E., and Griffiths, P. T.: Influence of sea ice-derived halogens on atmospheric HO_x as observed in
616 Springtime coastal Antarctica, *Geophys. Res. Lett.*, 46, 10168-10176, [https://doi.
617 org/10.1029/2019GL083825](https://doi.org/10.1029/2019GL083825), 2019.

618 Casado, M., Landais, A., Masson-Delmotte, V., Genthon, C., Kerstel, E., Kassi, S., Arnaud, L., Picard, G., Prie, F., Cattani,
619 O., Steen-Larsen, H. -C., Vignon, E., and Cermak, P.: Continuous measurements of isotopic composition of water
620 vapour on the East Antarctic Plateau, *Atmos. Chem. Phys.*, 16(13), 8521-8538, [https://doi.org/10.5194/acp-16-8521-
621 2016](https://doi.org/10.5194/acp-16-8521-2016), 2016.

622 Casciotti, K.L., Sigman, D.M., Hastings, M.G., Böhlke, J.K. and Hilkert, A.: Measurement of the oxygen isotopic composition
623 of nitrate in seawater and freshwater using the denitrifier method, *Anal. chem.*, 74(19), 4905-4912,
624 <https://doi.org/10.1021/ac020113w>, 2002.

625 Chuck, A. L., Turner, S. M., and Liss, P. S.: Direct evidence for a marine source of C₁ and C₂ alkyl nitrates, *Science*, 297,
626 1151-1154, <https://doi.org/10.1126/science.1073896>, 2002.

627 Collett, K. S., Piketh, S. J., and Ross, K. E.: An assessment of the atmospheric nitrogen budget on the South African Highveld,
628 *S. Afr. J. Sci.*, 106(5/6), 1-9, <http://dx.doi.org/10.4102/sajs.v106i5/6.220>, 2010.

629 Dahl, E. E., and Saltzman, S. E.: Alkyl nitrate photochemical production rates in North Pacific seawater, *Mar. Chem.*, 112,
630 137-141, <https://doi.org/10.1016/j.marchem.2008.10.002>, 2008.

631 Dahl, E. E., Heiss, E. M., and Murawski, K.: The effects of dissolved organic matter on alkyl nitrate production during
632 GOMECC and laboratory studies, *Mar. Chem.*, 142, 11-17, <https://doi.org/10.1016/j.marchem.2012.08.001>, 2012.

633 Dahl, E. E., Saltzman, S. E., and de Bruyn, W. J.: The aqueous phase yield of alkyl nitrates from ROO + NO: Implications for
634 photochemical production in seawater, *Geophys. Res. Lett.*, 30(6), 1-4, <https://doi.org/10.1029/2002GL016811>, 2003.

635 Dahl, E. E., Yvon-Lewis, S. A., and Saltzman, S. E.: Saturation anomalies of alkyl nitrates in the tropical Pacific Ocean,
636 *Geophys. Res. Lett.*, 32(L20817), 1-4, <https://doi.org/10.1029/2005GL023896>, 2005.

637 Dar, S. S., Ghosh, P., Swaraj, A., and Kumar, A.: Craig-Gordon model validation using observed meteorological parameters
638 and measured stable isotope ratios in water vapor over the Southern Ocean, *Atmos. Chem. Phys.*, 20(19), 11435-
639 11449, <https://doi.org/10.5194/acp-20-11435-2020>, 2020.

640 Davidson, E. A., and Kinglerlee, W.: A global inventory of nitric oxide emissions from soils, *Nutr. Cycling Agroecosyst.*, 48,
641 37-50, <https://doi.org/10.1023/A:1009738715891>, 1997.

642 Elliott, E. M., Kendall, C., Wankel, S. D., Burns, S. A., Boyer, E. W., Harlin, K., Bain, D. J., and Butler, T. J.: Nitrogen
643 isotopes as indicators of NO_x source contributions to atmospheric nitrate deposition across the Midwestern and
644 Northeastern United States, *Environ. Sci. Technol.*, 41(22), 7661-7667, <https://doi.org/10.1021/es070898t>, 2007.

645 Erbland, J., Vicars, W. C., Savarino, J., Morin, S., Frey, M. M., Frosini, D., Vince, E., and Martins, J. M. F.: Air-snow transfer
646 of nitrate on the East Antarctic Plateau - Part 1: Isotopic evidence for a phytotically driven dynamic equilibrium in
647 summer, *Atmos. Chem. Phys.*, 13(13), 6403-6419, <https://doi.org/10.5194/acp-13-6403-2013>, 2013.

648 Fang, Y. T., Koba, K., Wang, X. M., Wen, D. Z., Li, J., Takebayashi, Y., Liu, X. Y., and Yoh, M.: Anthropogenic imprints on
649 nitrogen and oxygen isotopic composition of precipitation nitrate in a nitrogen-polluted city in southern China, *Atmos.*
650 *Chem. Phys.*, 11, 1313-1325, <https://doi.org/10.5194/acp-11-1313-2011>, 2011.

651 Finlayson-Pitts, B. J., and Pitts, J. N.: *Chemistry of the upper and lower troposphere*. San Diego, California: Academic Press,
652 2000.

653 Fisher, J. A., Atlas, E. L., Barletta, B., Meinardi, S., Blake, D. R., Thompson, C. R., Ryerson, T. B., Peischl, J., Tzompa-Sosa,
654 Z. A., and Murray, L. T.: Methyl, ethyl and propyl nitrates: global distribution and impacts on reactive nitrogen in
655 remote marine environments, *J. Geophys. Res. Atmos.*, 123(21), 412-429, <https://doi.org/10.1029/2018JD029046>,
656 2018.

657 Frey, M. M., Savarino, J., Morin, S., Erbland, J., and Martins, J. M.: Photolysis imprint in the nitrate stable isotope signal in
658 snow and atmosphere of East Antarctica and implications for reactive nitrogen cycling, *Atmos. Chem. Phys.*, 9, 8681-
659 8696, <https://doi.org/10.5194/acp-9-8681-2009>, 2009.

660 Freyer, H. D.: Seasonal variation of $^{15}\text{N}/^{14}\text{N}$ ratios in atmospheric nitrate species, *Tellus B: Chem. Phys. Meteorol.*, 43(1), 30-
661 44, <https://doi.org/10.1034/j.1600-0889.1991.00003.x>, 1991.

662 Freyer, H. D., Kley, D., Volz-Thomas, A., and Kobel, K.: On the interaction of isotopic exchange processes with
663 photochemical reactions in atmospheric oxides of nitrogen, *J. Geophys. Res. Atmos.*, 98(D8), 14791-14796,
664 <https://doi.org/10.1029/93JD00874>, 1993.

665 Freyer, H. D., Kobel, K., Delmas, R. J., Kley, D., and Legrand, M. R.: First results of $^{15}\text{N}/^{14}\text{N}$ ratios in nitrate from alpine and
666 polar ice cores, *Tellus B: Chem. Phys. Meteorol.*, 48(1), 93-105, <https://doi.org/10.3402/tellusb.v48i1.15671>, 1996.

667 Gobel, A. R., Altieri, K. E., Peters, A. J., Hastings, M. G., and Sigman, D. M.: Insights into anthropogenic nitrogen deposition
668 to the North Atlantic investigated using the isotopic composition of aerosol and rainwater nitrate, *Geophys. Res. Lett.*,
669 5977-5982, <https://doi.org/10.1002/2013GL058167>, 2013.

670 Grannas, A. M., Jones, A. E., Dibb, J., Ammann, M., Anastasio, C., Beine, H. J., Bergin, M., Bottenheim, J., Boxe, C. S.,
671 Carver, G., Chen, G., Crawford, J. H., Domine, F., Frey, M. M., Guzman, M. I., Heard, D. E., Hemig, D., Hoffmann,
672 M. R., Honrath, R. E., Huey, L. G., Hutterli, M., Jacobi, H. W., Klan, P., Lefer, B., McConnell, J., Plane, J., Sander,
673 R., Savarino, J., Shepson, P. B., Simpson, W. R., Sodeau, J. R., von Glasow, R., Weller, R., Wolff, E. W., and Zhu,
674 T.: An overview of snow photochemistry: evidence, mechanisms and impacts, *Atmos. Chem. Phys.*, 7(2), 4165-4283,
675 <https://doi.org/10.5194/acp-7-4329-2007>, 2007.

676 Grasshoff, K., Kremling, K., & Ehrhardt, M.: *Methods of seawater analysis*, Verlag Chemi, Florida, 1983.

677 Guha, T., Lin, C. T., Bhattacharya, S. K., Mahajan, A. S., Ou-Yang, C.-F., Lan, Y.-P., Hsu, S. C., and Liang, M.-C.: Isotope
678 ratios of nitrate in aerosol samples from Mt. Lulin, a high altitude station in Central Taiwan, *Atmos. Environ.*, 154,
679 53-69, <http://dx.doi.org/10.1016/j.atmosenv.2017.01.036>, 2017

680 Guilpart, E., Vimeux, F., Evan, S., Brioude, J., Mertzger, J., Barthe, C., Risi, C., and Cattani, O.: The isotopic composition of
681 near-surface water vapor at the Maïdo observatory (Reunion Island, southwestern Indian Ocean) documents the

682 controls of the humidity of the subtropical troposphere, *J. Geophys. Res. Atmos.*, 122, 9628-9650,
683 <https://doi.org/10.1002/2017JD026791>, 2017.

684 Hamilton, D. S., Lee, L. A., Pringle, K. J., Reddington, C. L., Spracklen, D. V., and Carslaw, K. S.: Occurrence of pristine
685 aerosol environments on a polluted planet, *PNAS*, 111(52), 18466-18471, <https://doi.org/10.1073/pnas.1415440111>,
686 2014.

687 Hastings, M. G., Sigman, D. M., & Lipschultz, F.: Isotopic evidence for source changes of nitrate in rain at Bermuda, *J.*
688 *Geophys. Res. Atmos.*, 108(D24), <https://doi.org/10.1029/2003JD003789>, 2003.

689 Haywood, J., and Boucher, O.: Estimates of the direct and indirect radiative forcing due to tropospheric aerosols: a review,
690 *Rev. Geophys.*, 513-543, <https://doi.org/10.1029/1999RG000078>, 2000.

691 Hoering, T.: The isotopic composition of the ammonia and the nitrate ion in rain, *Geochim. Cosmochim. Acta.*, 12(1-2), 97-
692 102, [https://doi.org/10.1016/0016-7037\(57\)90021-2](https://doi.org/10.1016/0016-7037(57)90021-2), 1957.

693 IPCC 2013: Boucher, O. D., Randall, P., Artaxo, C., Bretherton, G., Feingold, P., Forster, V.-M., Kerminen, Y., Kondo, H.,
694 Liao, U., Lohmann, P., Rasch, S.K., Satheesh, S., Sherwood, B., Stevens, and Zhang, X. Y.: Clouds and Aerosols, in:
695 *Climate Change 2013: The Physical Science Basis. Contribution of Working Group I to the Fifth Assessment Report*
696 *of the Intergovernmental Panel on Climate Change*, edited by: Stocker, T.F., Qin, D., Plattner, G.-K., Tignor, M.,
697 Allen, S. K., Boschung, J, Nauels, A., Xia, Y., Bex, V., and Midgley, P. M., Cambridge University Press, Cambridge,
698 United Kingdom and New York, NY, USA, 2013.

699 Ishino, S., Hattori, S., Savarino, J., Jourdain, B., Preunkert, S., Legrand, M., Caillon, N., Barbero, A., Kurlbayashi, N., and
700 Yoshida, N.: Seasonal variations of triple oxygen isotopic compositions of atmospheric sulfate, nitrate and ozone at
701 Durmont d'Urville, coastal Antarctica, *Atmo. Chem. Phys.*, 17, 3713-3727, [https://doi.org/10.5194/acp-17-3713-](https://doi.org/10.5194/acp-17-3713-2017)
702 2017, 2017.

703 Jacobi, H.-W., and Schrems, O.: Peroxyacetyl nitrate (PAN) distribution over the South Atlantic Ocean,
704 *Phys. Chem. Chem. Phys.*, 1, 5517-5521, <https://doi.org/10.1039/A905290I>, 1999.

705 Jacobi, H.-W., Weller, R., Jones, A. E., Anderson, P. S., and Schrems, O.: Peroxyacetyl nitrate (PAN) concentrations in the
706 Antarctic troposphere measured during the photochemical experiment at Neumayer (PEAN'99). *Atmos. Environ.*, 34,
707 5235-5247, [https://doi.org/10.1016/S1352-2310\(00\)00190-4](https://doi.org/10.1016/S1352-2310(00)00190-4), 2000.

708 Jiang, S., Shi, G., Cole-Dai, J., Geng, L., Ferris, D. G., An, C., and Li, Y.: Nitrate preservation in snow at Dome A, East
709 Antarctica from ice core concentration and isotope records, *Atmos. Environ.*, 213, 405-412,
710 <https://doi.org/10.1016/j.atmosenv.2019.06.031>, 2019.

711 Johnston, J. C., & Thiemens, M. H.: The isotopic composition of tropospheric ozone in three environments. *J. Geophys. Res.*
712 *Atmos.*, 102(D21), 25395-25404, <https://doi.org/10.1029/97JD02075>, 1997.

713 Jones, A. E., Weller, R., Anderson, P. S., Jacobi, H.-W., Wolff, E. W., Schrems, O., and Miller, H.: Measurements of NO_x
714 emissions from the Antarctic snowpack, *Geophys. Res. Lett.*, 28(8), 1499-1502,
715 <https://doi.org/10.1029/2000GL011956>, 2001.

716 Jones, A. E., Weller, R., Minikin, A., Wolff, E. W., Sturges, W. T., McIntyre, H. P., Leonard, S. R., Schrems, O., and Bauguutte,
717 S.: Oxidized nitrogen chemistry and speciation in the Antarctic troposphere, *J. Geophys. Res. Atmos.*, 104(D17),
718 21355-21366, <https://doi.org/10.1029/1999JD900362>, 1999.

719 Jones, A. E., Weller, R., Wolff, E. W., and Jacobi, H.-W.: Speciation and rate of photochemical NO and NO₂ production in
720 Antarctic snow, *Geophys. Res. Lett.*, 27(3), 345-348, <https://doi.org/10.1029/1999GL010885>, 2000.

721 Kamezaki, K., Hattori, S., Iwamoto, Y., Ishino, S., Furutani, H., Miki, Y., Uematsu, M., Miura, K., and Yoshida, N.: Tracing
722 the sources and formation pathways of atmospheric particulate nitrate over the Pacific Ocean using stable isotopes,
723 *Atmos. Environ.*, 209, 152-166, <https://doi.org/10.1016/j.atmosenv.2019.04.026>, 2019.

724 Kendall, C., Elliot, E. M., and Wankel, S. D.: Tracing anthropogenic inputs of nitrogen to ecosystems, in: *Stable isotopes in
725 ecology and environmental science*, edited by: Michener, R., & Lajtha, K., Blackwell Publishing, Malden, Mass 375-
726 449, <https://doi.org/10.1002/9780470691854.ch12>, 2007.

727 Kim, M. J., Michaud, J. M., Williams, R., Sherwood, B. P., Pomeroy, R., Azam, F., Burkart, M., and Bertram, T. H.: Bacteria-
728 driven production of alkyl nitrates in seawater, *Geophys. Res. Lett.*, 42, 597-604,
729 <https://doi.org/10.1002/2014GL062865>, 2015.

730 Krankowsky, D., Bartecki, F., Klees, G. G., Mauersberger, K., and Schellenbach, K.: Measurement of heavy isotope
731 enrichment in tropospheric ozone, *Geophys. Res. Lett.*, 22(13), 1713-1716, <https://doi.org/10.1029/95GL01436>,
732 1995.

733 Kroopnick, P., and Craig, H.: Atmospheric oxygen: isotopic composition and solubility fractionation, *Science*, 175(4017), 54-
734 55, 1972.

735 Lee, H.-M., Henze, D. K., Alexander, B., and Murray, L. T.: Investigating the sensitivity of surface-level nitrate seasonality
736 in Antarctica to primary sources using a global model, *Atmos. Environ.*, 89, 757-767,
737 <http://dx.doi.org/10.1016/j.atmosenv.2014.03.003>, 2014.

738 Michalski, G., Bhattacharya, S. K., and Mase, D. F.: Oxygen isotope dynamics of atmospheric nitrate and its precursor
739 molecules, in: *Handbook of environmental isotope geochemistry. Advances in Isotope Geochemistry*, edited by:
740 Baskaran, M., Springer, Berlin, Heidelberg, 613-635, https://doi.org/10.1007/978-3-642-10637-8_30, 2012.

741 Michalski, G., Scott, Z., Kabilig, M., and Thiemens, M. H.: First measurements and modeling of $\Delta^{17}\text{O}$ in atmospheric nitrate,
742 *Geophys. Res. Lett.*, 30(9), <https://doi.org/10.1029/2003GL017015>, 2003.

743 Monks, P. S.: Gas-phase radical chemistry in the troposphere, *Chem. Soc. Rev.*, 34, 376-395,
744 <https://doi.org/10.1039/B307982C>, 2005.

745 Morin, S., Savarino, J., Frey, M. M., Domine, F., Jacobi, H. W., Kaleschke, L., and Martins, J. M.: Comprehensive isotopic
746 composition of atmospheric nitrate in the Atlantic Ocean boundary layer from 65°S to 79°N, *J. Geophys. Res. Atmos.*,
747 114(D05303), 1-19, <https://doi.org/10.1029/2008JD010696>, 2009.

748 Nadzir, M. S., Ashfold, M. J., Khan, M. F., Robinson, A. D., Bolas, C., Latif, M. T., Wallis, B. M., Mead, M. I., Hamid, H. H.
749 A., Harris, N. R. P., Ramly, Z. T. A., Lai, G. T., Liew, J. N., Ahamed, F., Uning, R., Samah, A. A., Maulud, K. N.,

750 Suparta, W., Zainudin, S. K., Wahab, M. I. A., Sahani, M., Müller, M., Yeok, F. S., Rahman, N. A., Mujahid, A.,
751 Morris, K. I. and Sasso, N. D.: Spatial-temporal variations in surface ozone over Ushuaia and the Antarctic region:
752 observations from in situ measurements, satellite data, and global models, *Environ. Sci. Pollut. Res.*, 25, 2194-2210,
753 <https://doi.org/10.1007/s11356-017-0521-1>, 2018.

754 Nesbitt, S. W., Zhang, R., and Orville, R. E.: Seasonal and global NO_x production by lightning estimated from the Optical
755 Transient Detector (OTD), *Tellus B: Chem. Phys. Meteorol.*, 52(5), 1206-1215,
756 <https://doi.org/10.3402/tellusb.v52i5.17098>, 2000.

757 Park, S. S., and Kim, Y. J.: Source contributions to fine particulate matter in an urban atmosphere, *Chemosphere*, 59, 217-226,
758 <https://doi.org/10.1016/j.chemosphere.2004.11.001>, 2005.

759 Park, Y., Park, K., Kim, H., Yu, S., Noh, S., Kim, M.-S., Kim, J.-Y., Ahn, J.-Y., Seok, K.-S., and Kim, Y.-H.: Characterizing
760 isotopic compositions of TC-C, NO₃⁻-N and NH₄⁺-N in PM_{2.5} in South Korea: Impact of China's winter heating,
761 *Environ. Pollut.*, 233, 735-744, <https://doi.org/10.1016/j.envpol.2017.10.072>, 2018.

762 Rindelaun, J. D., McAvey, K. M., and Shepson, P. B.: The photochemical production of organic nitrates from α -pinene and
763 loss via acid-dependent particle phase hydrolysis, *Atmos. Environ.*, 100, 193-201,
764 <https://doi.org/10.1016/j.atmosenv.2014.11.010>, 2015.

765 Rolph, G. D.: Real-time Environmental Applications and Display System (READY) Website (<http://www.ready.noaa.gov>).
766 NOAA Air Resources Laboratory, College Park, MD, 2016.

767 Savarino, J., Kaiser, J., Morin, S., Sigman, D. M., and Thiemens, M. H.: Nitrogen and oxygen isotopic constraints on the origin
768 of atmospheric nitrate in coastal Antarctica, *Atmos. Chem. Phys.*, 7, 1925-1945, [https://doi.org/10.5194/acp-7-1925-](https://doi.org/10.5194/acp-7-1925-2007)
769 [2007](https://doi.org/10.5194/acp-7-1925-2007), 2007.

770 Scarchilli, C., Frezzotti, M., and Ruti, P. M.: Snow precipitation at four ice core sites in East Antarctica: provenance,
771 seasonality and blocking factors, *Clim. Dyn.* 37, 2107-2125, <https://doi.org/10.1007/s00382-010-0946-4>, 2011.

772 Schumann, U., and Huntrieser, H.: The global lightning induced nitrogen oxides source, *Atmos. Chem. Phys.*, 7(1), 2623-
773 2818, <https://doi.org/10.5194/acp-7-3823-2007>, 2007.

774 Shi, G., Buffen, A. M., Hastings, M. G., Li, C., Ma, H., Li, Y., Sun, B., An, C., and Jiang, S.: Investigating the post-depositional
775 processing of nitrate in East Antarctic snow: isotopic constraints in photolytic loss, re-oxidation, and source inputs,
776 *Atmos. Chem. and Phys.*, 15, 9435-9453, <https://doi.org/10.5194/acp-15-9435-2015>, 2015.

777 Shi, G., Buffen, A. M., Ma, H., Hu, Z., Sun, B., Li, C., Yu, J., Ma, T., An, C., Jiang, S., Li, Y., and Hastings, M. G.:
778 Distinguishing summertime atmospheric production of nitrate across the East Antarctic ice sheet,
779 *Geochim. Cosmochim. Acta.*, 231, 1-14, <https://doi.org/10.1016/j.gca.2018.03.025>, 2018.

780 Shi, G., Ma, H., Zhu, Z., Hu, A., Chen, Z., Jiang, Su., An, C., Yu, J., Ma, T., Li, Y., Sun, B., and Hastings, M. G.: Using stable
781 isotopes to distinguish atmospheric nitrate production and its contribution to the surface ocean across hemispheres,
782 *Earth Planet. Sci. Lett.*, 564, 1-12, <https://doi.org/10.1016/j.epsl.2021.116914>, 2021.

783 Sigman, D.M., Casciotti, K.L., Andreani, M., Barford, C., Galanter, M. and Böhlke, J.K.: A bacterial method for the nitrogen
784 isotopic analysis of nitrate in seawater and freshwater, *Anal. Chem.*, 73(17), 4145-4153,
785 <https://doi.org/10.1021/ac010088e>, 2001.

786 Sinclair, K. E., Bertler, N. A. N., Trompeter, W. J., and Baisden, W. T.: Seasonality of airmass pathways to coastal Antarctica:
787 ramifications for interpreting high-resolution ice core records, *J. Clim.*, 26(6), 2065-2076,
788 <https://doi.org/10.1175/JCLI-D-12-00167.1>, 2013.

789 Spreen, G., Kaleschke, L., and Heygster, G.: Sea ice remote sensing using AMSR-E 89-GHz channels,
790 *J. Geophys. Res. Oceans*, 113(C02S03), 1-14, <https://doi.org/10.1029/2005JC003384>, 2008.

791 Stein, A.F., Draxler, R.R., Rolph, G.D., Stunder, B.J.B., Cohen, M.D., and Ngan, F.: NOAA's HYSPLIT atmospheric transport
792 and dispersion modeling system, *Bull. Amer. Meteor. Soc.*, 96, 2059-2077, <https://doi.org/10.1175/BAMS-D-14-00110.1>, 2015.

794 Thiemens, M. H.: History and applications of mass-independent isotope effects. *Annu. Rev. Earth Planet. Sci.*, 34, 217-262,
795 <https://doi.org/10.1146/annurev.earth.34.031405.125026>, 2006.

796 van der A, R. J., Eskes, H. J., Boersma, K. F., van Noije, T. P., Van Roozendaal, M., De Smedt, I., Peters, D. H. M. U., and
797 Meijer, E. W.: Trends, seasonal variability and dominant NO_x source derived from a ten year record of NO₂ measured
798 from space, *J. Geophys. Res. Atmos.*, 113, 1-12, <https://doi.org/10.1029/2007JD009021>, 2008.

799 Vicars, W. C., and Savarino, J.: Quantitative constraints on the ¹⁷O-excess ($\Delta^{17}\text{O}$) signature of surface ozone: Ambient
800 measurements from 50°N to 50°S using the nitrite-coated filter technique, *Geochim. Cosmochim. Acta.*, 135, 270-
801 287, <https://doi.org/10.1016/j.gca.2014.03.023>, 2014.

802 Virkkula, A., Teinila, K., Hillamo, R., Kerminen, V. M., Saarikoski, S., Aurela, M., Viidanoja, J., Paatero, J., Koponen, I. K.,
803 and Kulmala, M.: Chemical composition of boundary layer aerosol over the Atlantic Ocean and at an Antarctic site,
804 *Atmos. Chem. Phys.*, 6(11), 3407-3421, <https://doi.org/10.5194/acp-6-3407-2006>, 2006.

805 Walters, W. W., and Michalski, G.: Theoretical calculation of nitrogen isotope equilibrium exchange fractionation factors for
806 various NO_y molecules, *Geochim. Cosmochim. Acta.*, 164, 284-297, <http://dx.doi.org/10.1016/j.gca.2015.05.029>,
807 2015.

808 Walters, W. W., and Michalski, G.: Theoretical calculation of oxygen equilibrium isotope fractionation factors involving
809 various NO_y molecules, OH, and H₂O and its implications for isotope variations in atmospheric nitrate,
810 *Geochim. Cosmochim. Acta.*, 191, 89-101, <http://dx.doi.org/10.1016/j.gca.2016.06.039>, 2016.

811 Walters, W. W., Michalski, G., Böhlke, J. K., Alexander, B., Savarino, J., and Thiemens, M. H.: Assessing the seasonal
812 dynamics of nitrate and sulfate aerosols at the South Pole utilizing stable isotopes, *J. Geophys. Res. Atmos.*, 124(14),
813 8161-8177, <https://doi.org/10.1029/2019JD030517>, 2019.

814 Walters, W. W., Simonini, D. S., and Michalski, G.: Nitrogen isotope exchange between NO and NO₂ and its implications for
815 $\delta^{15}\text{N}$ variations in tropospheric NO_x and atmospheric nitrate, *Geophys. Res. Lett.*, 43, 440-448,
816 <https://doi.org/10.1002/2015GL066438>, 2016.

- 817 Weller, R., Jones, A. E., Wille, A., Jacobi, H.-W., McIntyre, H. P., Sturges, W. T., Huke, M., and Wagenback, D.: Seasonality
818 of reactive nitrogen oxides (NO_y) at Neumayer Station, Antarctica, *J. Geophys. Res. Atmos.* 107(D23), 1-11,
819 <https://doi.org/10.1029/2002JD002495>, 2002.
- 820 Williams, J. E., Le Bras, G., Kukui, A., Ziereis, H., and Brenninkmeijer, C. A. M.: The impact of the chemical production of
821 methyl nitrate from the $\text{NO} + \text{CH}_3\text{O}_2$ reaction on the global distributions of alkyl nitrates, nitrogen oxides and
822 tropospheric ozone: a global modelling study. *Atmos. Chem. Phys.*, 14(5), 2363-2382, [https://doi.org/10.5194/acp-](https://doi.org/10.5194/acp-14-2363-2014)
823 [14-2363-2014](https://doi.org/10.5194/acp-14-2363-2014), 2014.
- 824 Yeatman, S. G., Spokes, P. F., Dennis, P. F., and Jickells, T. D.: Comparisons of aerosol nitrogen isotopic composition at two
825 polluted coastal sites, *Atmos. Environ.*, 35, 1307-1320, [https://doi.org/10.1016/S1352-2310\(00\)00408-8](https://doi.org/10.1016/S1352-2310(00)00408-8), 2001.
- 826 Zong, Z., Wang, X., Tian, C., Chen, Y., Fang, Y., Zhang, F., Li, C., Sun, J., Li, J., and Zhang, G.: First assessment of NO_x
827 sources at a regional background site in North China using isotopic analysis linked with modeling,
828 *Environ. Sci. Technol.*, 51, 5923-5931, <https://doi.org/10.1021/acs.est.6b06316>, 2017.